photonics

MDPI

Review

Regulating Terahertz Photoconductivity in Two-Dimensional Materials

Xiao Xing [1,†], Zeyu Zhang [2,†] and Guohong Ma [3,*]

[1] Center for Transformative Science, ShanghaiTech University, Shanghai 201210, China; xingxiao@shanghaitech.edu.cn
[2] School of Physics and Optoelectronic Engineering, Hangzhou Institute for Advanced Study, University of Chinese Academy of Sciences, Hangzhou 310024, China; zhangzeyu@ucas.ac.cn
[3] Department of Physics, Shanghai University, Shanghai 200444, China
* Correspondence: ghma@staff.shu.edu.cn
† These authors contributed equally to this work.

Abstract: Two-dimensional materials represented by graphene have attracted extensive interest owing to the unique layer-dependent physical properties that are tunable with various external fields. In addition, by stacking two or more 2D materials together, a new material with the desired properties can be tailored and designed. Fully understanding the dynamical photoconductive response in 2D materials is uttermost important to design and develop the advanced optoelectronic devices. Terahertz (THz) time-domain spectroscopy (TDS) and time-resolved THz spectroscopy are powerful spectroscopic tools with the advantages of being contact-free and noninvasive, which have been widely used to study the photoconductivity (PC) of 2D materials. In this review, firstly, we provide a short introduction of the 2D materials and THz spectroscopy, and then a brief introduction of the experimental setup and experimental data analysis based on time-resolved THz spectroscopy are presented. After that, we overview the latest progress on the regulation of the THz PC that includes: (1) regulating the THz PC of graphene (Gr) and transition metal dichalcogenide (TMD) thin films with oxygen adsorption; (2) regulating the THz PC of Gr and Gr/TMDs heterostructures by electric gating and a built-in field introduced by a substrate; (3) regulating the THz PC of Gr/TMD heterostructures via optical gating; and (4) we overview the latest progress on the observation of elementary excitations in 2D materials with THz PC spectra following optical excitation and THz PC regulation via the photoexcitation of quasi-particles. Finally, we conclude the review and present a short overview of future research directions.

Keywords: terahertz; two-dimensional materials; photoconductivity; graphene; transition metal dichalcogenides; heterostructure

check for updates

Citation: Xing, X.; Zhang, Z.; Ma, G. Regulating Terahertz Photoconductivity in Two-Dimensional Materials. *Photonics* **2023**, *10*, 810. https://doi.org/10.3390/photonics10070810

Received: 22 May 2023
Revised: 27 June 2023
Accepted: 8 July 2023
Published: 12 July 2023

Copyright: © 2023 by the authors. Licensee MDPI, Basel, Switzerland. This article is an open access article distributed under the terms and conditions of the Creative Commons Attribution (CC BY) license (https://creativecommons.org/licenses/by/4.0/).

1. Introduction

Since the discovery of single-layer graphene in 2004 [1], the emerging two-dimensional materials have fundamentally changed the landscape of materials science [2–5]. Owing to its unique properties, high stability in air, high tunability, and easy availability, studies on 2D materials have increased in the last 20 years [1–8]. Two-dimensional materials consist of a wide range of materials, in which the constituent atoms are strongly coupled with covalent bonds in plane and weakly coupled through van der Waals (vdW) interactions in the out-of-plane direction. In addition to the main material of graphene (Gr), the most studied 2D materials also include transition metal dichalcogenides (TMDs) [9], hexagonal boron nitride (hBN) [10], silicene (2D silicon) [11], MXene (2D carbide/nitrides) [12], phosphorene [13], and borophene (2D boron) [14], as well as the heterostructure constructed by stacking two or more monolayer 2D materials together with a particular stacking sequence [3,7,15,16]. Most 2D materials have a hexagonal structure; thus, it is possible to stack them with other 2D materials to enrich their properties.

Two-dimensional materials provide a powerful platform for exploring fundamental science and have several potential applications. Moreover, tunability and comparability make 2D materials and their heterostructures promising candidates for finding new materials and designing advanced devices in the field of electronics, optoelectronics, and photonics, such as photo-transistors [17,18], solar cells [19], light-emitting diodes [20], photodetectors [21], modulators, switches, and flexible electronics [22]. In a 2D material, the (photo-)carriers are confined in a two-dimensional space that results in interesting properties that the bulk counterpart does not have, such as large exciton binding energy, vast enhancement of optical nonlinearity, rich quantum freedoms (for instance, spin, pseudospin, and valleytronic), and novel states of matter (e.g., Ising superconductivity and 2D magnetism). These quantum degrees of freedom as well as their coupling with light, electric, and magnetic fields have initiated novel physical phenomena in 2D materials. In addition, 2D heterostructures constructed with 2D materials are no longer limited by lattice-matching conditions, an atomic interdiffusion that was required in traditional heterostructures, thus providing a unique platform for the development of optoelectronic devices. The application of 2D materials in various electronic and photonic devices requires an in-depth understanding of carrier dynamics in both equilibrium and non-equilibrium states. THz spectroscopy has been demonstrated to be a powerful spectroscopic tool to explore the static and non-equilibrium state of carriers in a contactless way.

Briefly, THz radiation refers to the electromagnetic wave band with frequency that ranges from 0.1 THz to 10 THz, which corresponds to the photoenergy range from 0.4 meV to 40 meV and a wavelength range from 3 mm to 30 μm [23–27]. The THz band falls between low-frequency electronics and high-frequency photonics: Considering the working frequency of gigahertz in most modern microelectronic devices, it is desired to develop high-speed electronic device working in the THz frequency. On the other hand, comparing the low photon energy to visible light, THz radiation is very sensitive to the free carrier around the Fermi surface, which makes THz spectroscopy a crucial tool for accessing carrier dynamics in addition to transient absorption spectroscopy. THz time-domain spectroscopy (TDS) can provide the real and imaginary parts of complex conductivity simultaneously without referring to Kramers–Kronig relation. Optical pump and THz probe (OPTP) spectroscopy is a powerful tool to explore the photocarrier dynamics of condensed matters that has been applied to access the dynamical THz PC in 2D materials [24,27]. The OPTP can directly access the relaxation dynamics of photoexcited carriers, including radiation and non-radiation recombination. As a low photon energy spectroscopy with sub-ps time resolution, OPTP is a unique tool to assess the intraband scattering by analyzing time-dependent complex PC, through which a clear and conclusive carrier transport picture can be obtained [27]. In addition, different materials show distinct spectral signatures that are relevant to the pump fluence, wavelength, and temperature, as well as delay time between pump and THz pulses, and the complex THz PC can be used to address fundamental questions, such as dynamical charger transfer and subsequent relaxation, formation and relaxation of low-energy elementary excitation, and the mode hybridization of different collective excitations. From an application point of view, the dynamic THz PC also can provide an alternative way to design high-speed modulators, switches, as well as photo-transistors.

In this article, we provide a comprehensive review of the investigations into regulating THz PC in ultrathin 2D-layered materials as well as their heterostructures. Following this brief introduction, we provide a short description of the experimental setup, including THz time-domain spectroscopy and time-resolved THz spectroscopy, as well as the physical models used to analyze the experimental data. Then, we overview the latest progress on regulating THz PC in 2D materials from four perspectives: In Section 3, we review the influence of gas absorption on THz PC in graphene and TMDs films, in which we mainly discuss the effect of oxygen absorption on the thin films' PC. In Section 4, we review the impact of electric gating on THz PC in graphene as well as the tuning of THz PC in Gr/TMD heterostructures by a built-in field introduced by a substrate. In Section 5, we provide an

overview on the regulation of THz PC in Gr/TMD heterostructures via photogating. In Section 6, we discuss the regulation of THz PC via the photoinduced formation of novel elementary excitations, such as trion, small polaron, and large polaron. Finally, we conclude the review with a discussion on the potential applications of 2D materials based on PC, and a short outlook is also presented discussing the rapidly developing research in this field.

2. THz Experimental Setup and THz Data Analysis

A typical optical pump and THz probe (OPTP) spectroscopy are displayed schematically in Figure 1 [28,29]. An ultrafast laser pulse train is delivered from a femtosecond laser with a typical pulse duration of ~100 fs and pulse energy of a few mJ. The BS1 is used to split the laser beam into two beams, the reflection beam passes through an optical parametric amplifier (OPA), and the output wavelength from OPA is tunable from ultraviolet to visible to near and middle infrared that acts as a pump beam. The BS2 is used to further split the transmitted beam into the THz generation beam and the THz detection beam. The reflection beam from BS2 is focused on a (110)-oriented ZnTe crystal to generate a THz pulse via optical rectification. The generated THz radiation is then collimated and focused by a pair of off-axis parabolic mirrors PM1 and PM2 on the surface of the sample. The THz pulse through the sample is collimated and focused by another pair of parabolic mirrors PM3 and PM4 on the another (110)-oriented ZnTe wafer, in which the transient electric field of THz pulse is obtained via free-space electro-optical sampling. The weak sampling beam is detected with a balanced photodetector that is connected to a lock-in amplifier. The phase of the lock-in amplifier is locked to an optical chopper that modulates either the THz generation arm or the pump beam at a typical frequency of 500 Hz. The THz beam is enclosed and purged with dry nitrogen to avoid water vapor absorption.

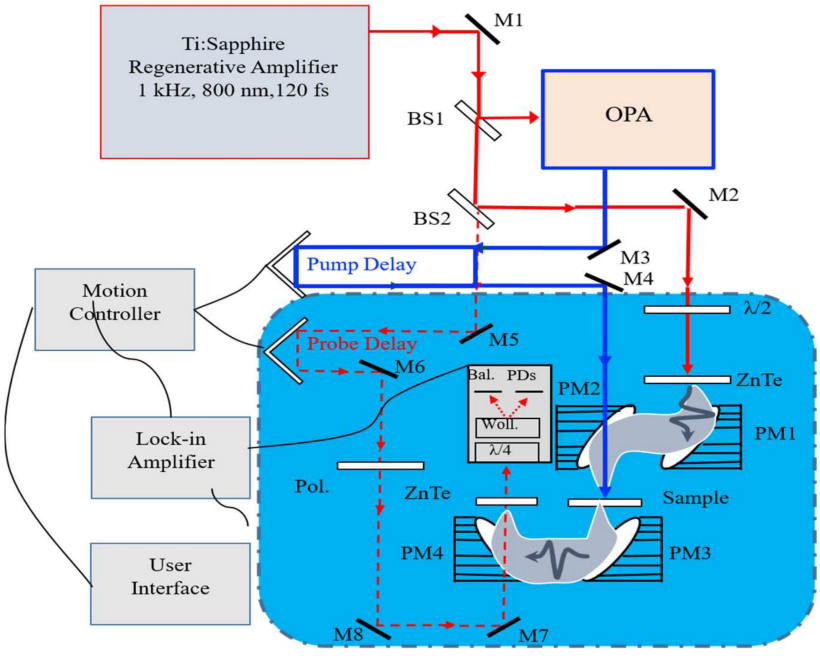


Figure 1. Experimental arrangement for time-resolved THz spectroscopy and THz time-domain spectroscopy (highlighted blue square area). BS: beam splitter; M: reflection mirror; PM: off-axis parabolic mirror; Pol: polarizer; λ/2: half-wave plate; λ/4: quarter-wave plate; Woll: Wollaston prism; Bal. PDs: balanced photodiodes.

It should be noted that the spot size of the pump beam on the sample position should be at least two-times larger than that of the THz beam whilst conducting the OPTP experiment, which ensures a relatively uniform photoexcited region for the sample of THz probe. In addition, the thickness of the sample should be much smaller than the penetration depth $1/\alpha$, with α of absorption coefficient. In the experimental setup shown in Figure 1, what can

be measured includes: (i) Adjusting the probe delay line ensures that the transmitted THz electric field is fixed around the peak value, and then the dynamical relaxation of the THz PC of the sample can be obtained by scanning the pump delay time. (ii) By fixing the delay time between the pump pulse and the THz probe pulse, the transmitted THz wavefront can be sampled by scanning the probe delay line, and the complex THz PC dispersion ($\Delta\sigma = \Delta\sigma_r + i\Delta\sigma_i$) is then obtained by applying a fast Fourier transform. Assuming that a thin film with a thickness d is supported on a substrate with a thickness d_s, the THz transmission ($T(\omega, t)$) is defined as the ratio between the transmitted THz electric fields with the pump pulse at the delay time t ($E_{on}(\omega, t)$) and without a pump ($E_0(\omega, t)$). Under thin-film approximation, $T(\omega, t)$ reads [28,29]:

$$T(\omega, t) = \frac{E_{on}(\omega, t)}{E_0(\omega, t)} = \frac{1 + n_s}{1 + n_s + Z_0 \Delta\sigma d} = A(\omega, t)e^{i\varphi} \quad (1)$$

Obviously, $A(\omega, t)$ is the amplitude ratio of the Fourier-transformed THz signal for the excited sample at the delay time t and the unexcited sample, and φ is the phase difference between them. n_s and Z_0 are the refractive indexes of the substrate and free-space impedance, with $Z_0 \approx 377\ \Omega$. Then, the THz PC at the delay time t is expressed by:

$$\Delta\sigma(\omega, t) = \frac{1 + n_s}{Z_0 d}\left(1 - \frac{1}{T(\omega, t)}\right) = -\frac{1 + n_s}{Z_0 d}\frac{\Delta T(\omega, t)}{T_0(\omega)} = -\frac{1 + n_s}{Z_0 d}\frac{\Delta E(\omega, t)}{E_0(\omega)} \quad (2)$$

where $\Delta T = T - T_0$ and $\Delta E = E_{on} - E_0$ with $T(E_{on})$ and T_0 (E_0) of the complex THz transmission (electric field) with and without a pump, respectively. Accordingly, in the complex THz PC, $\Delta\sigma = \Delta\sigma_r + i\Delta\sigma_i$ of the real ($\Delta\sigma_r$) and imaginary ($\Delta\sigma_i$) parts of THz PC is then expressed by:

$$\Delta\sigma_r(\omega, t) = \left(\frac{\cos\varphi}{A(\omega, t)} - 1\right)\frac{1 + n_s}{Z_0 d} \quad (3a)$$

$$\Delta\sigma_i(\omega, t) = -\frac{(1 + n_s)\sin\varphi}{A(\omega, t)Z_0 d} \quad (3b)$$

The frequency and delay-time dependence of the real and imaginary parts of PC is manifestation of the photocarrier transportation of materials. Conventionally, THz PC dispersion can be modelled using Drude model [30,31], Drude–Smith model [32], and Drude–Lorentz model [30,31], depending on the photocarrier scattering mechanisms. The Drude model describes the free carrier response with an average momentum scattering rate, Γ:

$$\Delta\sigma = \frac{D}{\Gamma - i\omega} \quad (4)$$

where $D = Ne^2/m^*$ is Drude weight, with N, e, and m* denoting the photocarrier density, electron charge, and photocarrier effective mass, respectively. $\Gamma = 1/\tau$ and ω are, respectively, the momentum scattering rate and angular frequency with τ of the momentum scattering time. In order to extend the Drude model to a wide range of materials with a photocarrier localization, a modified Drude model was introduced by Smith; the Drude–Smith model is expressed by [32]:

$$\Delta\sigma = \frac{D\tau}{1 - i\omega\tau}\left(1 + \frac{c}{1 - i\omega\tau}\right) \quad (5)$$

where the constant c varies between 0 and -1, which presents the photocarrier backscattering effect, and sometimes it refers to the localization parameter of the photocarrier. It is clear that the Drude model is recovered with $c = 0$, and the full carrier localization effect becomes stronger when c approaches -1.

The Drude–Lorentz model is used to describe PC dispersion--involved quasi-free photocarrier and resonance feature in the spectra, which is a combination of the Drude model and the Lorentz model, which is expressed by:

$$\Delta\sigma = \frac{\varepsilon_0 \omega_p^2 \tau}{1 - i\tau\omega + i\omega_0^2/\omega} \quad (6)$$

where ω_p, τ, ε_0, and ω_0 are the plasma frequency, average momentum scattering time, vacuum permittivity, and the angular frequency of the oscillatory response, respectively. The Lorentz model is used to describe the low-frequency absorption modes, such as phonon, exciton, and plasmon.

In addition to the OPTP method, transient absorption (TA) and terahertz emission spectroscopy (TES) are also used to access the photocurrent and/or photoconductivity. Table 1 presents a comparison of the three methods for evaluating photoconductivity and/or photocurrent in 2D materials.

Table 1. The comparison of different time-resolved spectroscopy in 2D materials.

Time-Resolved Technique	Time Resolution	Spectra Range	Applicable Systems
OPTP	~500 fs	0.2–10 THz	Semiconducting, semimetal, and metallic systems
TA	~100 fs	Ultraviolet–Visible–Infrared	Exciton, plasmon, and optical phonon
TES	~100 fs	0.2–10 THz	Semiconducting, semimetal, and metallic systems

3. Regulating THz PC in 2D Materials by Gas Absorption

3.1. THz PC Regulation in Graphene by Gas Absorption

Since the discovery of the linear band dispersion and the Dirac electrons with Fermi velocity in graphene, the utilization of the Dirac electrons in 2D materials for information storage devices has been the focus of research [1]. In 2009, Zhang et al. reported that an applied voltage in bilayer graphene might open a gap in graphene [33], thus achieving the purpose of on-chip applications for the high-mobility Dirac electrons in 2D graphene. In 2012, as shown in Figure 2a, George et al. observed the negative THz PC in CVD-grown graphene following optical excitation, implying that graphene may have properties that are different from those of general semiconductors [34]. Planken's group attributed the light-induced transparency in graphene to the generation of stimulated THz radiation and successfully achieved THz emission by combining graphene with metal nanostructures, as illustrated in Figure 2b [35].

In 2014, Ivanov et al. suggested that the increase in light/THz-induced scattering rate and the decrease in in-band conductivity should be caused by the thermalization process of intraband carriers, as shown in Figure 2c,d [36]. That means that, after photoexcitation, the intraband-transition-induced hot carriers should thermalize the carriers near the Fermi surface, and then the chemical potential of graphene is modulated, resulting in the decrease in the conductivity near the Fermi surface. Based on the discussion about the intrinsic conductivity properties in graphene, the influence of external atmosphere on the THz conductivity of graphene is one important aspect. In 2012, Docherty et al. studied the photoinduced THz conductivity in the vacuum and an oxygen and nitrogen atmosphere, and the THz PC of graphene changed from negative to positive, as shown in Figure 3 [37]. At that time, this phenomenon was attributed to the fact that the graphene monolayer is modulated by the atmosphere, which induces the opening of the band gap and makes graphene a high mobility semiconductor.

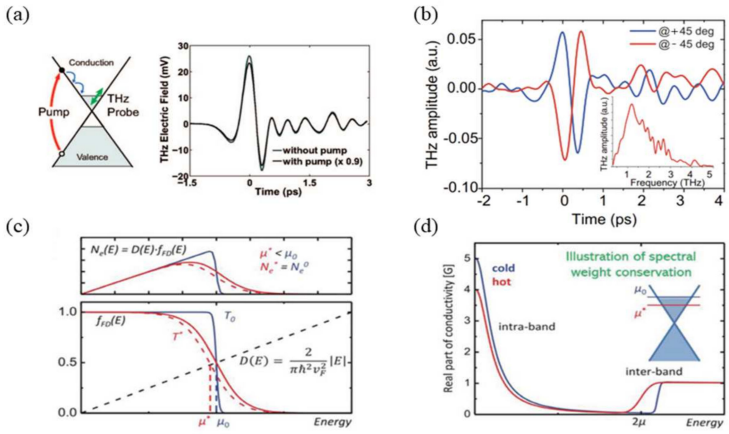


Figure 2. (**a**) The measured THz frequency pulses were transmitted through the epitaxial graphene without (gray) and with (black, scaled) an optical pump pulse preceding the peak of the THz pulse by 1 ps. (**b**) The time-domain THz radiation from a monolayer layer graphene on a glass slide. Both +45° (blue) and −45° (red) denote the incident angles of the pump beam. It should be noted that no THz radiation is detected at the incident angle of 0°. The inset shows the THz radiation in the frequency domain obtained by Fourier transformation (Reprinted with permission from Ref. [35]. Copyright 2014, American Chemistry Society). (**c**) Fermi–Dirac distribution before and after strong THz excitation. A smearing-out of the hot carrier distribution following optical thermalization shows a downshift of the chemical potential for maintaining the total carrier density [36]. (**d**) Illustration of spectral weight conservation in monolayer graphene. The decrease in chemical potential for hotter electrons leads to the increase in spectral weight for inter-band transitions, which is compensated by the decrease in the weight of the intra-band absorption of graphene (Reprinted with permission from Ref. [36]. Copyright 2015, Institute of Physics).

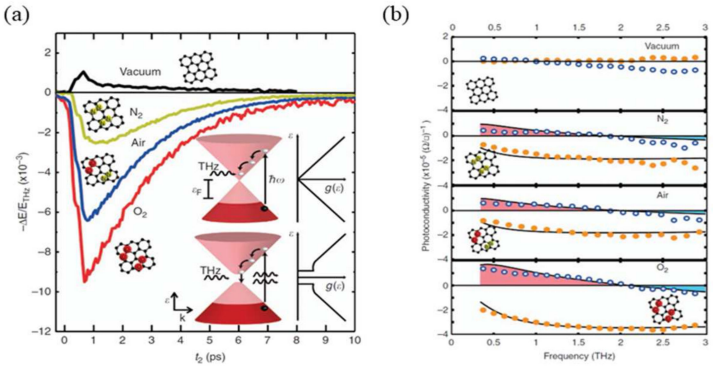


Figure 3. (**a**) Environmental dependence of pump-induced changes in THz PC. (**b**) THz PC spectra of graphene in different environments (Reprinted with permission from Ref. [37]. Copyright 2015, Springer Nature).

In 2017, Zhang et al. reported the physical understanding of THz PC modulation in CVD-grown graphene after photoexcitation in different atmospheres. The photoinduced THz PC cooling process was shown to be modulated by the physical adsorption of different gas molecules at the graphene surface [38]. Figure 4 demonstrates that O_2 absorption leads to decease in Fermi level of graphene, which is equivalent to the optical pump. By using the thermodynamic model, they demonstrated that the Fermi level of graphene can be modulated by adsorbing gas molecules, leading to a decrease in the chemical potential of graphene, and as a result, a decrease in THz PC can be expected [39]. Consequently, the decrease in THz PC can also be achieved by increasing the pump fluence. Microscopically, efficient electron–electron interactions convert the energy of the current into the heat energy of graphene's entire electron gas almost instantaneously, which elevates the electronic temperature, smears out of the Fermi–Dirac distribution, and lowers the electron gas

chemical potential. This further results in a reduced conductivity in the THz-frequency band [40]. Based on the reproducibility of the gas adsorption experiments, the relationship between THz conductivity and atmosphere in graphene can be mainly attributed to the physical adsorption of gas molecules on the graphene surface [41]. The characteristic of the Fermi level modulation by physical adsorption had also been applied to graphene-based gas sensors [42].

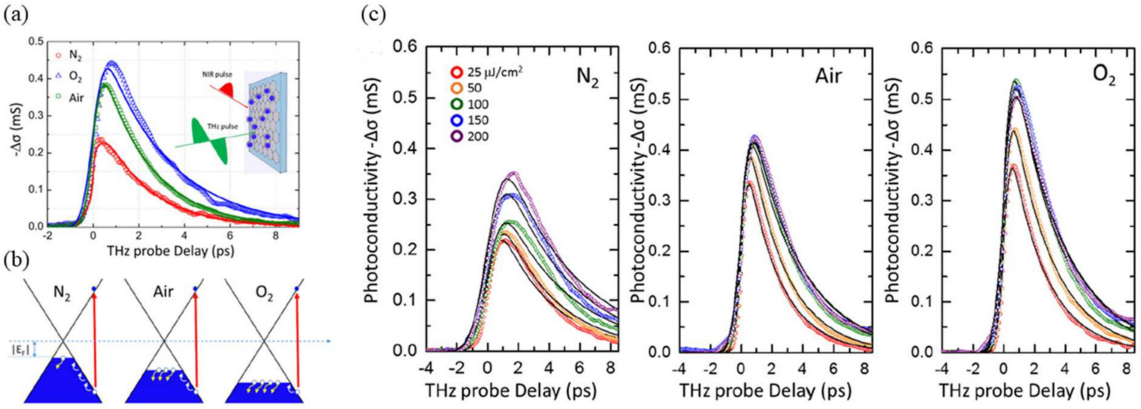


Figure 4. (**a**) Transient THz PC in N_2, air, and O_2 gaseous conditions. (**b**) The illustration of the Fermi level of graphene in the three gas environments. (**c**) Transient THz PC under various pump fluences in N_2, air, and O_2 conjunction with a single exponential fitting (solid lines) [38]. (Reprinted with permission from Ref. [38]. Copyright 2017, American Institute of Physics).

3.2. THz PC Regulation in TMDs Using Gas Absorption

The use of 2D materials in technological applications has gained increasing attention in recent decades. The tunable and layer-dependent bandgap, chemical and thermal stability, and mechanical strength make 2D TMDs viable potential components for emerging electronic devices [43–47]. In addition, the photoluminescence spectrum of TMDs can be adapted in various ways, including chemical doping [48] and class of substrate [49] and dielectric environment [50] choice, amongst others [51]. Because of their high surface-to-volume ratio, TMDs have excellent sensing potential. Numerous studies have focused on how the surroundings impact mono- and few-layer TMD devices [52,53]. Specifically, MoS_2 sensitivity to NO and NO_2 has been demonstrated [54]. It has also been shown that the conduction type of WSe_2 is highly sensitive to pressure [52]. Notably, studies suggest that $PdSe_2$ acts as an excellent gas sensor [53].

In their single-layer form, TMDs enable enhanced gate control in easy-to-fabricate transistors that are immune to short-channel effects. The ability to modulate either *n*-type or *p*-type charge transport is a key advantage of TMD transistors [55]. For example, Park et al. [56] and Qiu et al. [57] reported that adsorbed O_2 substantially reduces the current in MoS_2 field effect transistors (FETs). Grillo et al. investigated the influence of air pressure upon the carrier mobility of multilayer $PtSe_2$ back-gated FET: the *p*-type $PtSe_2$ FET exhibited positive PC under high vacuum in contrast to a negative PC when the pressure is raised [58]. In addition, just as the O_2 "photo-cleaning" effect observed in graphene [58,59], Zhang et al. reported that the observed, higher *n*-doped behavior in CVD-grown MoS_2 turned to *p*-dopants following laser ablation in an oxygen atmosphere [60–62]. Additionally, Tongay et al. demonstrated that the *n*-dopants in MoS_2 can be neutralized by atmospheric adsorbates [63,64]. Furthermore, the attachment of gaseous molecules has a substantial impact on the optical profiles of MoS_2. For instance, adsorbed gases can strengthen the photoluminescence of monolayer MoS_2 [65], and adsorbed O_2 modulates the dielectric function of monolayer MoS_2 [66].

The effect of O_2 on the THz PC of these 2D materials could be crucial for device realization. As shown in Figure 5, Xing et al. observed that the THz PC of a single layer of molybdenum disulfide changed with the ambient gas: negative in nitrogen and positive in

air/oxygen. This provides a simple method for regulating the photoelectric properties of 2D materials [67]. The phenomenon of THz PC tuning is more likely to occur in an *n*-doped MoS_2. After photoexcitation, in the presence of oxygen, the mechanism of THz PC in MoS_2 monolayers changes from being dominated by trions to being dominated by free-charge carriers [68,69].

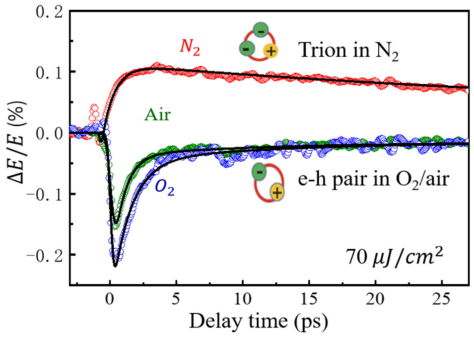


Figure 5. Transient-pump-induced THz transmission of monolayer MoS_2 in N_2 (red), air (green), and O_2 (blue) under pump fluence of 70 μJ/cm^2. Positive THz transmission in N_2 indicates photoinduced negative PC, and negative THz transmission in O_2 and air suggest photoinduced positive PC. Solid curves show a bi-exponential fitting [67].

Gustafson et al. [70] also investigated the influence of molecular oxygen on the PC of MoS_2 via transient THz spectroscopy. As shown in Figure 6, when the environment changes from a vacuum to atmospheric pressure, the THz photoconductive polarity of MoS_2 transitions from negative to positive. They attributed this behavior to the physical adsorption of O_2 from the *n*-type MoS_2 using extra electrons [70].

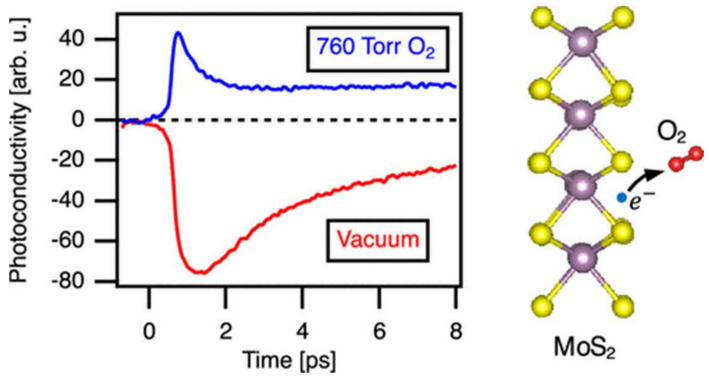


Figure 6. THz PC of monolayer MoS_2 in a vacuum and in 760 Torr O_2 as a function of time after pump excitation [70].

4. Regulating THz PC in 2D Materials with Electrostatic Gating

4.1. Regulating THz PC of Graphene with Electrostatic Gating

Charge carrier in graphene exhibits high mobility and strong interaction with electromagnetic radiation over a wide range of frequencies [71,72], which provides a good platform for testing electronic and optical response of 2D materials following optical excitation. In particular, OPTP spectroscopy provides access to a transient THz PC response. It was noted that positive THz PC was demonstrated in epitaxial graphene on a SiC substrate [73], while negative THz PC was observed in graphene-grown fused silica and quartz substrates by chemical vapor deposition (CVD) [74–76]. It has been thought that the negative THz PC in CVD-grown graphene may arise from THz-stimulated emission with optical excitation [77]. Later, it was noted that the vast difference between epitaxial-growth graphene shows very-low intrinsic carrier density, while the CVD-grown graphene conventionally shows *p*-doped with a much lower Fermi energy level. As a result, people argued

that the opposite THz PC observed in graphene fabricated with different technique arises from their different charge densities [78–80]. Therefore, regulating THz PC is applicable by adjusting the intrinsic carrier density, i.e., the Fermi level of graphene, which has been studied extensively in recent decades. At present, it is clear that graphene shows positive THz PC when the Fermi level is close to the Dirac point, i.e., neutral charge graphene, in which carrier interband scattering plays a dominating role following optical excitation. On the other hand, graphene shows negative THz PC when the Fermi level is distant from the Dirac point that corresponds to doped graphene; in this case, the carrier intraband scattering accounts for the observed negative PC. In order to observe the transition from the positive PC to a negative one in graphene, a popular method uses OPTP spectroscopy combined with electrostatic gating.

In 2014, Frenzel et al. [78] reported the semiconducting-to-metallic PC crossover in graphene by using the electrostatic gating method. In the same year, Shi et al. [79] conducted a similar study. Figure 7 schematically illustrates the key concept that the authors attempted to study. By adjusting the gating voltage V_g, the doping carrier density can be controlled; as a result, the negative-to-positive THz PC is controllable, which can be clearly seen with OPTP spectroscopy.

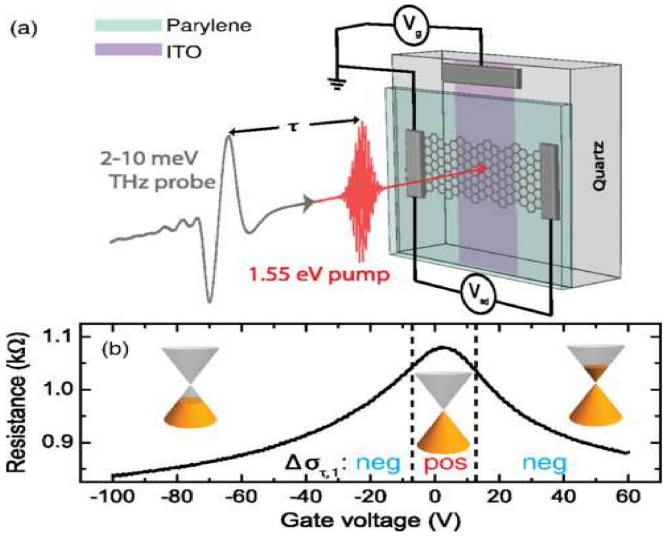


Figure 7. Regulating THz PC with electrostatic gating. (**a**) Illustration of transparent graphene geometry and optical pump and THz probe measurement. (**b**) Gating voltage V_g-dependent resistance of the device. The maximum resistance corresponds to a gating voltage of $V_g = V_{CN} = 3$ V, in which the hole doping is about $p = 1.7 \times 10^{11}$ cm^{-2}. The voltage between the two vertical dash lines corresponds to the crossover gating voltage of positive-to-negative THz PC (Reprinted with permission from Ref. [78]. Copyright 2014, American Physical Society).

The biased, dependent THz PC of the graphene device was measured with a conventional OPTP spectroscopy at room temperature in high vacuum. The sample was photoexcited with a 100 fs laser pulse at a central wavelength of 800 nm. The typical experimental results are shown in Figure 8, in which the transmitted THz pulse is collected at the condition of the pump fluence of 10 μJ/cm^2 with biased voltages of $V_g - V_{CN} = 2$ V and $V_g - V_{CN} = 52$ V. It is obvious from Figure 8a that the change in the transmitted THz field (ΔE) shows an opposite sign to that of the incident THz pulse for the case of $V_g - V_{CN} = 2$ V, reflecting a photo-enhanced THz absorption. The extracted THz PC dispersion, $\Delta\sigma = \Delta\sigma_R(\omega) + i\Delta\sigma_{Im}(\omega)$, shows a positive real part ($\Delta\sigma_R(\omega) > 0$) (Figure 8b). In direct contrast, ΔE shows the same sign as that of the incident THz pulse when $V_g - V_{CN} = 52$ V, as shown in Figure 8c, which reveals the photoinduced decrease in THz absorption; correspondingly, the extracted real part of THz PC is negative, as expected ($\Delta\sigma_R(\omega) < 0$) (Figure 8d). Figure 8e shows the transient THz electric field transmission with various biases, which clearly demonstrates that the transmitted THz field changes with the applied

bias. By considering the interplay between photoinduced carrier population change (Δn) and scattering rate (Γ), the authors modelled the THz PC dispersion, and the modelling results showed agreement with the experimental data qualitatively [78,79].

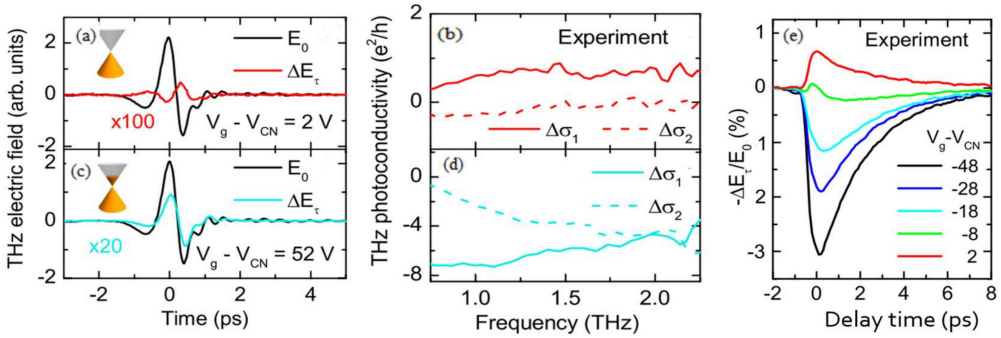


Figure 8. Gating voltage tuning of THz PC. (**a**) Transmitted THz waveform without a pump (black) and pump-induced THz waveform transmission change (red) around a delay time of 1.5 ps. (**b**) Real and imaginary components of transient THz PC extracted from the data in (**a**). (**c**,**d**) Experimental results under study are similar as those in (**a**,**b**), but at a gate voltage of $V_g = V_{CN} + 52$ V with $n \approx 3 \times 10^{12}$ cm^{-2}. (**e**) Transient THz PC measured at the peak of the signal in (**a**,**c**). All studies are conducted in a vacuum with a pump fluence of 10 μJ/cm^2 at room temperature (Reprinted with permission from Ref. [78]. Copyright 2014, American Physical Society).

Regarding the mechanism that governs the sign of THz PC in graphene, Tomadin et al. [80] performed a similar experimental study, and they reported similar experimental phenomena: the sign of THz PC transforms from negative at a near neutral charge doping to a positive one at a high charge doping. They presented an alternative explanation for the experimental data: The electronic screening plays a crucial role in the substrate-supported graphene thin film. In the case of charge neutrality, there is a greater free-carrier density available for conductance in the event of interband heating, and this pre-empts the effect of the reduced screening at a higher electron temperature. The THz PC is positive. For the highly doped graphene, where intraband scattering heating occurs, the system evolves to a state that weakens the shielding effect of substrate impurities, and the THz conductivity decreases with respect to the equilibrium value. The THz PC is negative. According to this non-regularized dynamical screening model, both carrier multiplication and interband recombination due to carrier–carrier scattering disappear [80].

Although electrostatic gating on graphene has been studied extensively, there is the challenge of regulating PC in few-layer TMDs via electric gating. For the semiconducting TMDs, such as $MoS(Se)_2$ and $WS(Se)_2$, the insulating nature of TMDs makes tuning carrier density in TMD difficult with a conventional voltage of a few volts to tens of volts. For (semi)metallic TMDs, such as WTe_2- and 1T′-phase $MoTe_2$, the electrical regulation of the TMDs could be limited by the challenges from the stacking and electrode growth technique of the heterostructures.

4.2. THz PC of Gr/TMD Heterostructures Regulated Using a Substrate Field

One of the most critical components of electronic or optoelectronic devices is the metal-semiconductor junction (MSJ) structure [81]. The Schottky barrier height (SBH, Φ), the energy barrier height for charge carrier transport across the junction, is a significant parameter for a MSJ that impacts device performance [82]. Efforts to tune Φ in 2D TMD-based devices have recently been increased because of their unique properties and photoelectric engineering applications [83–85]. However, experiments show that metals with different work functions have little effect on the Φ of metal–2D semiconductor heterojunctions, and the Fermi level of the heterojunction is essentially near the semiconductor band gap, with little change relative to the different metals used, and changing the type of metal has limited ability to regulate the Fermi level of the MSJ. Therefore, it is difficult to regulate Φ using different common metals because of the effect of Fermi level pinning (FLP) [86].

A recent study by Liu and colleagues [85] demonstrated that 2D metals present a viable solution to the challenging FLP problem. According to their findings, FLP is not effective for MSJs containing vdW interactions owing to the inhibition of metal-induced gap states in the semiconductor. As a result, the adjustment of the energy level alignment can be achieved using diverse 2D metals [86]. As shown in Figure 9, when the Fermi level is near to the lowest-lying states of the semiconductor, there is an energy difference $\Phi^0_{B,n}$ above the Fermi level, known as the *n*-type Schottky barrier contact, i.e., it is easier for electrons to flow from the semiconductor to the metal compared with flowing in the opposite direction. When the Fermi level is near to the highest-lying states of the semiconductor, there is an energy difference between the Fermi level and the valance band maximum (VBM), marked $\Phi^0_{B,p}$, i.e., *p*-type Schottky barrier contact, which controls the transport of holes across the MSJ interface [82].

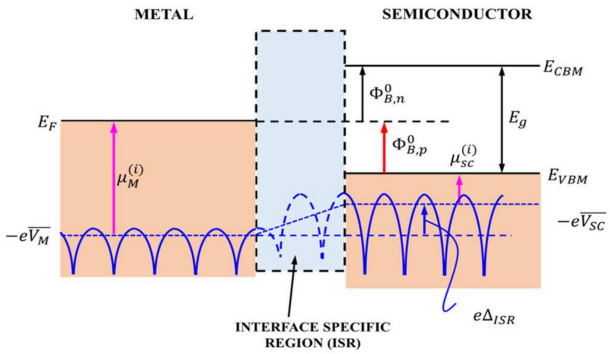


Figure 9. Band diagram at a metal–semiconductor interface [82].

Owing to its exceptional strength and excellent electrical and thermal conductivity, graphene has been widely used in various applications, including sensors, integrated circuits, and FETs [87–90]. In recent years, researchers have investigated numerous 2D heterostructures involving graphene and different materials, including but not limited to Gr/TMD heterostructures. Owing to its low electrical resistivity and high electron transfer rate, graphene effectively preserves its distinct attributes when combined with the intrinsic electronic characteristics of other 2D materials, such as Gr/TMDs heterostructures [91,92]. In Gr/TMD heterostructures, the SBH can be modified by applying a vertical electric field to the heterostructure. By applying an increasing vertical electric field to the Gr/WS_2 heterostructure, Zheng et al. observed a transition from an *n*-type to a *p*-type Schottky contact, indicating a significant change in the electronic properties of the material [93]. By adjusting the electric field, Yu et al. found that the Schottky barrier height of Gr/WSe_2 van der Waals heterostructures can be altered. This demonstrates that the electronic properties of the material can be manipulated using external forces [94]. A perpendicular electric field can modulate the electronic properties of the Gr/WSe_2 vdW heterostructure, as stated by Sun et al. [95].

For electronic and optoelectronic applications, interlayer coupling and charge transfer through the interface of Gr/TMD heterostructures play a critical role in modulating their electronic properties. However, it is not clear whether the charge transfer is electron or hole. Zhang et al. found that when light is absorbed by the MoS_2 layer in Gr/MoS_2 heterostructures, it generates electron–hole pairs that are subsequently separated across the layers. Specifically, the photoexcited electrons migrate from MoS_2 to graphene, while the photoexcited holes become trapped in the MoS_2 layer [96]. By using time-resolved OPTP spectroscopy, Xu et al. demonstrated that a Gr/WSe_2 heterostructure enabled the transfer of holes from WSe_2 to graphene, effectively lowering the Fermi level of graphene [97]. Zhu et al. verified that it is feasible to extract hot electrons from graphene post-carrier intraband scattering, but prior to the electron–hole interband thermalization. Their measurements showed a rapid electron injection (~25 fs) from graphene to WSe_2 when subjected to sub-bandgap excitation [98].

The influence of substrates on 2D materials is a result of charge transfer, doping monolayers, or dielectric screening [99]. The dielectric screening effect through substrates can impact both layers in a heterostructure as the charge screening length is greater than the thickness of the atomic layer [100]. In Gr/TMD heterostructures, the interfacial charge transfer can be affected by the effective electric field induced by the substrate [101–103]. For instance, in a Gr/WSe_2 heterostructure, the Dirac cone is commonly located adjacent to the valence band maximum of the WSe_2 layer. This configuration suggests the presence of a standard *p*-type Schottky barrier contact at the interface [95]. Xing et al. used OPTP spectroscopy to measure the ultrafast carrier dynamics in both WSe_2/Gr/sapphire (WSe_2/Gr) and Gr/WSe_2/sapphire (Gr/WSe_2) heterostructures. They performed this measurement by photoexciting the samples with photons of various energies spanning a range of 0.7–2.5 eV. The efficient electric field of the sapphire substrate induces a reduction in the electron barrier height in Gr/WSe_2, thereby transforming the Schottky barrier contact into an *n*-type. This alteration makes the transfer of photo-thermionic electrons from graphene to WSe_2 over the Schottky barrier more advantageous. Therefore, for photon energy values below the WSe_2 A-exciton excitation, i.e., only the graphene layer is excited, the relaxation time in Gr/WSe_2 is longer than that of graphene. However, in WSe_2/Gr, the barrier height for electrons increases, leading to a blocked photo-thermionic electron transfer. As a result, the lifetime of WSe_2/Gr is approximately similar to that of graphene (see Figure 10) [101].

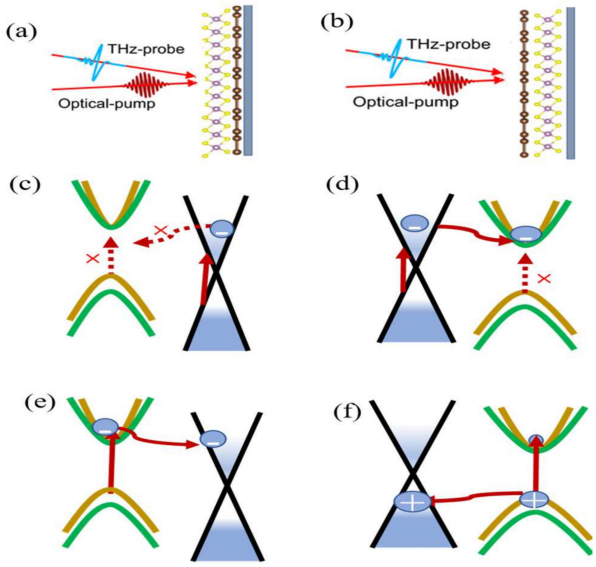


Figure 10. The study focused on exploring the dynamics of non-equilibrium hot carriers at the interface of Gr/WSe_2. To measure the PC of graphene, a time-resolved THz spectroscopy technique was used following photoexcitation in WSe_2/Gr (**a**) and Gr/WSe_2 (**b**). The CT process that occurs after sub-A-exciton excitation (such as 0.8 eV) in WSe2/Gr (**c**) and Gr/WSe2 (**d**) is depicted in the illustration. The above-A-exciton excitation (e.g., 2.5 eV) in WSe_2/Gr (**e**) and Gr/WSe_2 (**f**) leads to the direct transfer of electrons (or holes) at the interfaces, as illustrated in the schematic diagram [101].

Ma et al. explored the process of charge transfer in the heterojunction of five-layer $PtSe_2$/Gr, which was placed on a fused silica substrate. The findings presented in Figure 11 demonstrate that the direction of the electric field, which is consistently perpendicular to the substrate, can either facilitate or hinder the transfer of charges. Under a low pump fluence, the effective electric field introduced by the substrate promotes the transfer of photoexcited electrons in the $PtSe_2$/Gr/substrate configuration, resulting in negative THz PC. As the pump fluence increases, excess photo-generated carriers begin to screen the electric field introduced by the substrate, gradually causing the negative THz PC to transition into a positive one. In contrast, in the Gr/$PtSe_2$/substrate, no significant charge transfer can be detected, as indicated by the fact that the THz PC remains positive, regardless of the pump fluences applied and excitation wavelengths used [102]. The modulation of the electric

field induced by the substrate can alter the height of the Schottky barrier, thereby allowing the regulation of the THz PC.

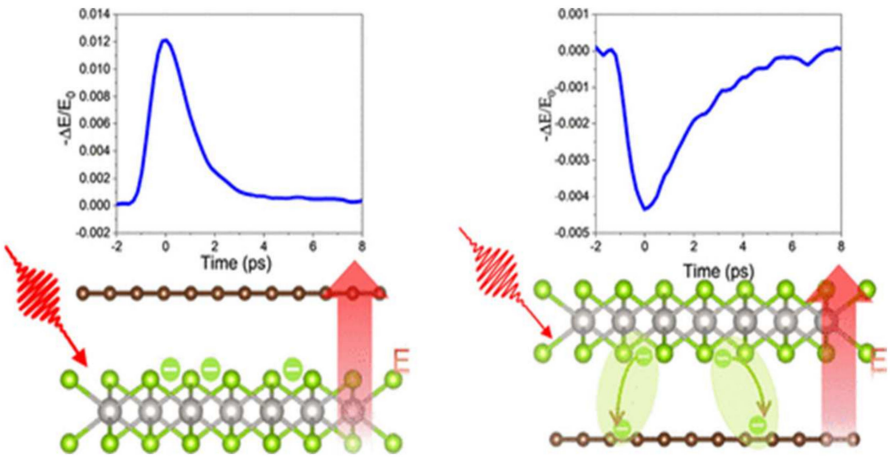


Figure 11. Transient THz PC of Gr/$PtSe_2$/substrate and $PtSe_2$/Gr/substrate. The diagrams illustrate how the effective field introduced by the substrate can impact the transfer of charges in Gr/$PtSe_2$/substrate and $PtSe_2$/Gr/substrate configurations (Reprinted with permission from Ref. [102]. Copyright 2021, American Chemistry Society).

5. Regulating THz PC in Gr/TMD Heterostructures by Photogating

In addition to gas adsorption and electric field by a substrate, a more direct way to regulate the PC of graphene is to use graphene-based 2D vdW heterojunctions. There are several methods to control the THz PC in such heterojunctions. In this paper, we first discuss the use of light itself to generate and control the positive and negative THz PC and, thus, verify the charge transfer process in 2D materials. In 2021, Fu et al. studied the charge transfer process in a Gr/WS_2 heterostructure with the OPTP technique for below and above band gap excitation [104]. As shown in Figure 12, they found that, when the heterojunction is excited below the bandgap of WS_2, the electron transfer occurs from graphene to WS_2. A direct hole transfer takes place from WS_2 to graphene by exciting heterojunctions above the WS_2 bandgap. The observed positive THz PC arises from the photogating effect on graphene. Considering that the carrier mobility of graphene is at least two-orders of magnitude higher than that of WS_2, the photoinduced charge transfer between graphene and WS_2 results in an increase in the hole concentration in graphene for both below and above band gap excitation. As a result, the THz PC is positive.

As shown in Figure 13a, Ma et al. [102] reported the changes in positive and negative THz PC in a $PtSe_2$/Gr heterojunction and found that the changes in positive and negative THz PC could be modulated by different stacking orders, which may be related to the formation of effective point fields by carriers' accumulation at the interface [102]. Later, in 2022, Quan et al. investigated this charge transfer method caused by carrier aggregation. It was found that it could be related to the charge transfer process caused by the thermal phonon bottleneck effect in graphene, with the analysis of the scattering time and the Smith parameter in the heterostructure, as shown in Figure 2b [105].

In 2022, Zou et al. reported that the process from negative to positive THz PC in the heterojunction between graphene and MoS_2 is related to the formation of interlayer excitons between graphene and MoS_2, and the formation time of such interlayer excitons was determined for the first time to be around 18 ps [106]. Furthermore, they also found the dependence of the laser fluence between the hot electron transport and photogating process by theoretical calculations. Figure 14 shows the dynamical formation of interlayer exciton in Gr/MoS_2 heterostructure under below and above bandgap excitation, investigated with transient spectroscopy and time resolved THz spectroscopy.

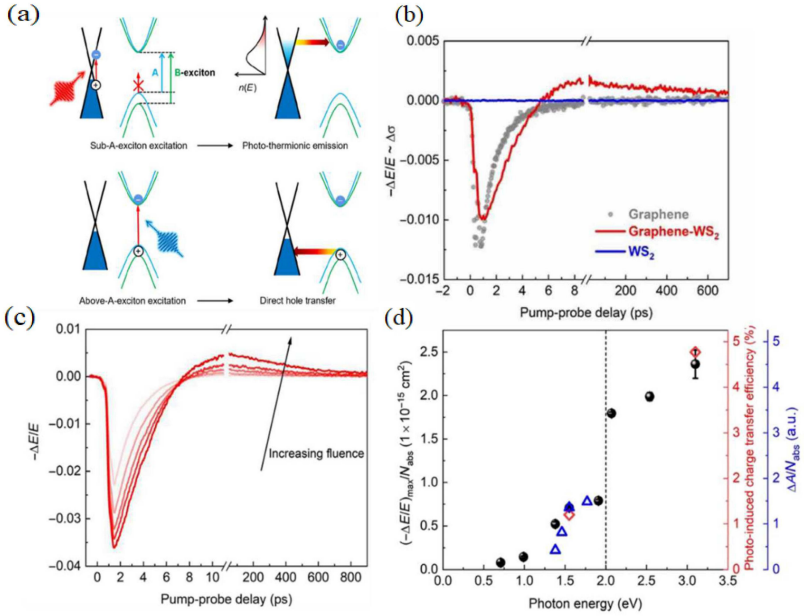


Figure 12. (**a**) Investigation on the non-equilibrium hot carrier dynamics at Gr/WS_2 interfaces. (**b**) Transient THz PC for graphene (gray), WS_2 (blue), as well as the Gr/WS_2 heterostructure (red). The measurement is conducted under dry N_2-purging conditions with a photon energy of 1.55 eV. (**c**) Transient THz PC for the Gr/WS_2 heterostructure with different pump fluences at a photon energy of 1.38 eV. (**d**) Calculated photon-energy-dependent efficiency of charge transfer in the Gr/WS_2 heterostructure. The black dots denote the "relative" charge transfer efficiency evaluated with transient THz data (the left Y-axis); the red diamonds are the absolute charge transfer efficiency obtained by THz TDS data (the right red Y-axis); the blue triangles refer to the relative charge transfer efficiency measured with transient absorption data under sub-A-exciton excitation (the right blue Y-axis) (Reprinted with permission from Ref. [104]. Copyright 2021, American Association for the Advancement of Science).

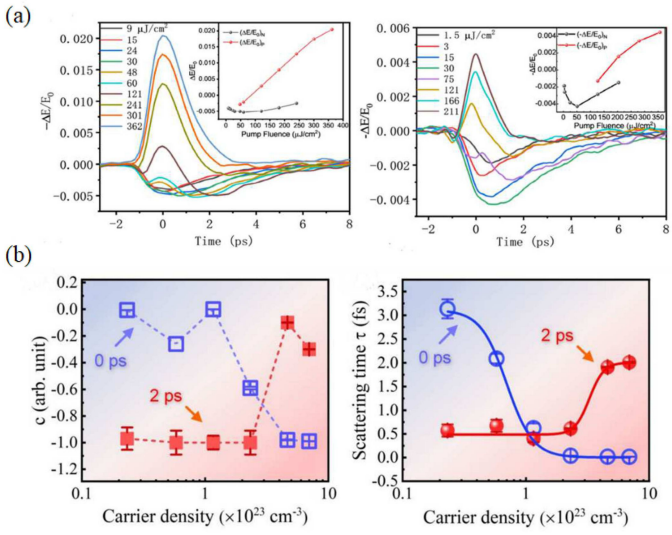


Figure 13. (**a**) Transient THz PC of the Gr/$PtSe_2$ heterostructure with various pump fluences at an excitation wavelength of 780 (**left** panel) and 1300 nm (**right** panel). The insets present the maximum modulation depth, $-\Delta E/E_0$, as a function of the pump fluence for 780 nm and 1300 nm, respectively. (**b**) Carrier density dependence of backscattering parameter c (**left** panel) and momentum scattering time τ (**right** panel) of the heterostructure at the delay times of 0 ps and 2 ps with 1300 nm excitation, respectively (Reprinted with permission from Ref. [105]. Copyright 2022, American Chemistry Society).

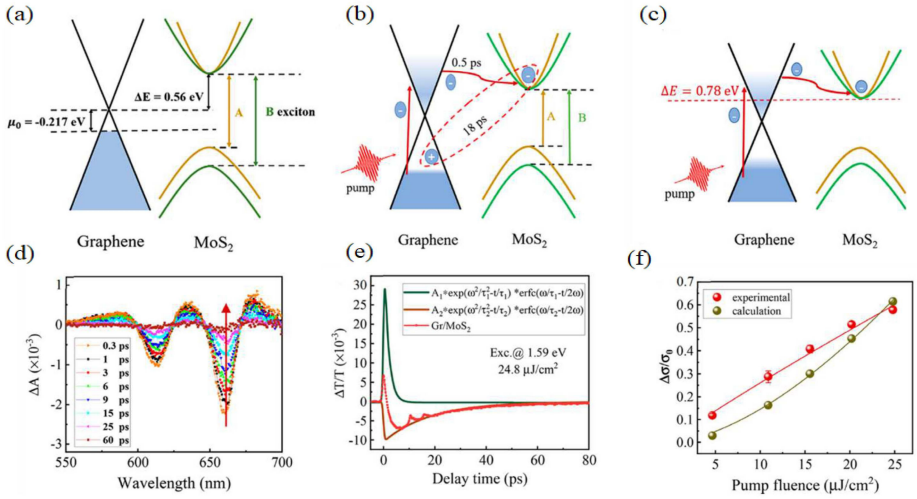


Figure 14. The illustrations of the band structure of the Gr/MoS_2 heterostructure (**a**), the interfacial exciton formation (**b**), and photogating process (**c**). (**d**) Representative TA spectra probed at several selected delay times. (**e**) Transient THz transmission of Gr/MoS_2 (red); green and yellow solid lines are bi-exponential fittings. (**f**) Pump-fluence-dependent number of transferred carriers. The red circles are obtained from the experimental data, which shows a sub-linearly dependence on the pump fluence, $\Delta\sigma/\sigma_0 \sim I^{0.9}$, while the green circles are the theoretical calculation, showing a superlinear pump fluence dependence, $\Delta\sigma/\sigma_0 \sim I^{1.6}$. (Reprinted with permission from Ref. [106]. Copyright 2022, American Chemistry Society).

To summarize, the photogating effect has been widely used to achieve the regulation of THz PC in graphene-based heterostructure, in which optical fluence, wavelength, as well as the heterostructure stacking order are the adjustable parameters to control the THz PC, including the sign and magnitude of the PC. It should be noted that the photogating effect could be applicable for mostly similar van der Waals structures. In addition, the photogating effect is also used to study the charge transfer process, such as the direction of charge transfer, the type of transferred carriers, and the amount of transferred carriers in graphene-based heterostructures [107]. This control can be considered as the photogating process of the Schottky barrier of the structure and has also been applied to graphene-based photodetectors.

6. Regulating THz PC in TMDs by the Photoinduced Formation of Elementary Excitation

THz PC can be used to probe the photoinduced formation of low-energy elementary excitations. The system lies at far out of equilibrium upon photoexcitation, so that the transport properties are very different from the equilibrium condition. The formation of low-energy elementary excitation following photoexcitation leads to a significant change in THz PC. Therefore, OPTP spectroscopy can be used to detect the newly formed quasi-particle, on the one hand, and the formation of the new quasi-particle results in the carrier mobility change that can be used to regulate the THz PC, on the other hand. In this paper, we briefly review the photoinduced formation of a trion (a charged exciton) and small and large polarons by using time-resolved THz spectroscopy.

6.1. Regulating THz Photoconductivity via the Formation of Trion in Monolayer MoS_2

Atomically thin transition dichalcogenides (TMDs) is a 2D semiconductor, which has been demonstrated to feature a strong quantum confinement and reduced dielectric screening effect [108–111]. The resulting strong Coulomb interaction causes the photoexcited electron–hole pairs to form tightly bound excitons, which determine the electronic and optical properties of the materials [109,111]. For most monolayer TMDs, unintentional doping is inevitable, which leads to TMDs with excess charges with *n*- or *p*-doping. Excitons formed by photoexcitation can capture additional charges to form trions, or charged

excitons [112,113]. These trions possess very different mobility as that of the excess charge carrier. As a result, the formation of trions can significantly affect the THz PC of the system [114]. Therefore, time-resolved THz spectroscopy is a sensitive tool to probe the formation of trions; vice versa, the formation of trions can also be used to regulate the THz PC.

Trion-induced negative THz PC was first studied in a monolayer MoS_2 by Lui et al. in 2014 [114]. The authors used a conventional optical pump and THz probe spectroscopy, in which a Ti: sapphire amplifier system generated a 90 fs laser pulse with a repetition rate of 5 kHz and a photon energy of 1.55 eV. The laser was split into two beams. One beam was guided into an optical parametric amplifier to output a frequency tunable pulse, which acts as a pumping beam. The other beam was used to generate THz radiation in the ZnTe crystal for probing the samples. The experiment was conducted in a high vacuum with a variable temperature. In this study, the monolayer MoS_2 on sapphire substrate was fabricated with the CVD method; the electron concentration and the carrier mobility in the monolayer MoS_2 were estimated to be ~$5.5 \pm 2 \times 10^{12}$ cm^{-2} and 180 ± 70 $cm^2V^{-1}s^{-1}$, respectively. The typical experimental results are shown in Figure 15, and Figure 15a presents the time-domain THz transmission of MoS_2/sapphire as well as a reference (bare sapphire). By referring to the sapphire substrate, the complex sheet conductivity of the monolayer MoS_2 can be obtained, from which the real part of average conductivity is $\sigma_1 \approx 2 \pm 0.5$ G_0 with $G_0 = 2e^2/h$ of the quantum of conductance. Following 400 nm optical excitation, the pump-induced change in THz transmission (proportional to ΔE) is shown in Figure 15b, and it is clear that the wavefront of ΔE shows the same sign as that of the incident THz pulse, which indicates that THz transmission is enhanced with pump excitation. Figure 15c further demonstrates this transient-pump-induced increase in THz transmission. It is clear that dynamical THz transmission exhibits a short component with a lifetime of 1 ps, followed by a long component with a lifetime of 42 ps. Figure 15d presents the extracted photoconductivity dispersion at a delay times of 3 ps (top panel) and 40 ps (down panel). It should be noted that both the real and imaginary parts of photoconductivity are negative for all delay times and in the investigated frequency.

The pump-induced negative THz PC in the monolayer MoS_2 is accounted for the formation of trions, which is depicted schematically in Figure 16 [114]. The monolayer MoS_2 film on the sapphire substrate fabricated with the CVD method behaves as an *n*-type semiconductor, which slightly attenuates the THz wave as illustrated in Figure 16a. With photoexcitation, the resulting electron–hole pairs form trions with the excess free charges on a very fast time scale. Trions behave as free charged particles with an increased effective mass, resulting in a reduced carrier mobility and reduced conductivity. As the photoexcitation does not increase the pure carrier concentration, instead, photoexcitation adds mass to the original free charges, leading to a decrease in conductivity and an increase in THz transmission, as illustrated in Figure 16c.

6.2. Regulating THz Photoconductivity by the Formation of Polarons

Similar to the formation of a trion via photoexcitation in a semiconductor, P. Suo et al. [115] reported the observation of negative THz photoconductivity in a Dirac semimetal $PtTe_2$ thin film with an optical pump and THz probe spectroscopy. The typical experimental findings are displayed in Figure 17, in which the $PtTe_2$ films with various thickness were fabricated by tellurizing Pt thin films on a fused silica substrate. Figure 17a shows the transient THz transmission, $\Delta T/T_0$ at 780 nm with a pump fluence of 542 $\mu J/cm^2$. The inset presents the zoomed-in view of a short time scale. It is obvious the transient transmission of THz frequency contains three phases with a different time scale: (1) a pump-induced rapid drop in THz amplitude transmission; (2) the rapid transition from positive to negative THz PC signal on sub-picosecond time scales; and (3) the slow recovery from the maximum bleaching signal to the equilibrium state. Figure 17b presents the dynamical evolution of THz transmission with various pump fluences. Considering that the bleaching signal lasts for a few *ns*, an exponential function convoluted with a laser pulse was used to fit the

transient THz transmission of Figure 17a in the initial 10 ps time window, and Figure 17c displays the fitting time constant with respect to the pump fluence. Figure 17d shows the transmitted THz waveforms through the film at the delay times of 0 ps (red) and 5 ps (blue) as well as without photoexcitation (black). By comparing with the transmitted THz waveform without pumping, the photoinduced change in the THz electric field, ΔE, shows to be out of phase at the zero delay time and in phase at the delay time of 5 ps. The in-phase characteristic for blue and black indicates the photoinduced bleaching in THz transmission, or rather, photoexcitation leads to the increase in THz transmission.

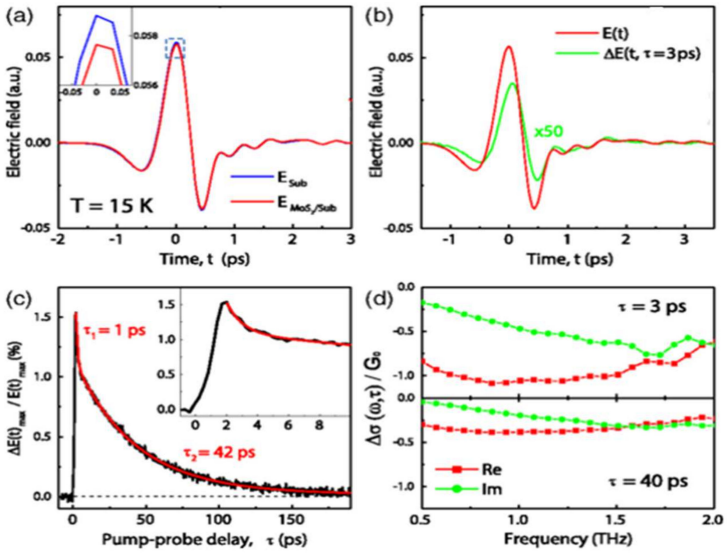


Figure 15. Observation of negative THz PC in the monolayer MoS_2 on a sapphire substrate. (**a**) THz transmission of MoS_2/sapphire (red) as well as the bare sapphire substrate (blue). The inset shows the zoomed-in view of the peak. (**b**) THz waveform transmission without a pump (red) and transmission change with a pump at the delay time of 3 ps (green). (**c**) Transient dynamics of the monolayer MoS_2 under a 400 nm pump. The red line is the fitting curve with bi-exponential function, yielding a lifetime of τ_1 = 3 ps and τ_2 = 42 ps. The inset shows the zoomed-in view of the short component. (**d**) Pump-induced complex conductivity change at the delay times of 3 ps and 40 ps. The experimental conditions: temperature T = 15 K; pump fluence of 50 μJ/cm^{2,} and pump photoenergy of 3.1 eV (Reprinted with permission from Ref. [114]. Copyright 2014, American Physical Society).

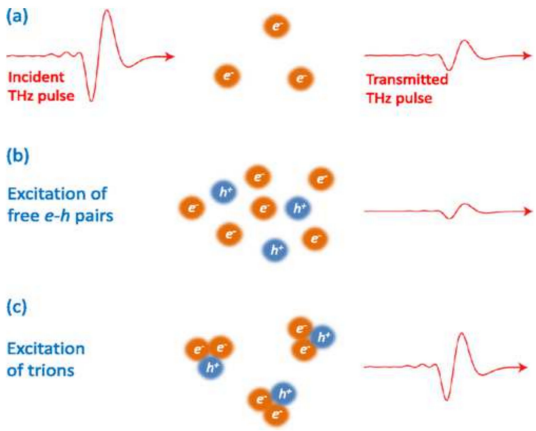


Figure 16. Illustration of trionic effect on the THz PC response in an *n*-doped semiconductor following above band gap photoexcitation. (**a**) Attenuation of THz radiation in an *n*-doping semiconductor. (**b**) Enhanced THz absorption after the photoexcitation of free electron–hole pairs. (**c**) Reduction in THz absorption by the formation of trions (Reprinted with permission from Ref. [114]. Copyright 2014, American Physical Society).

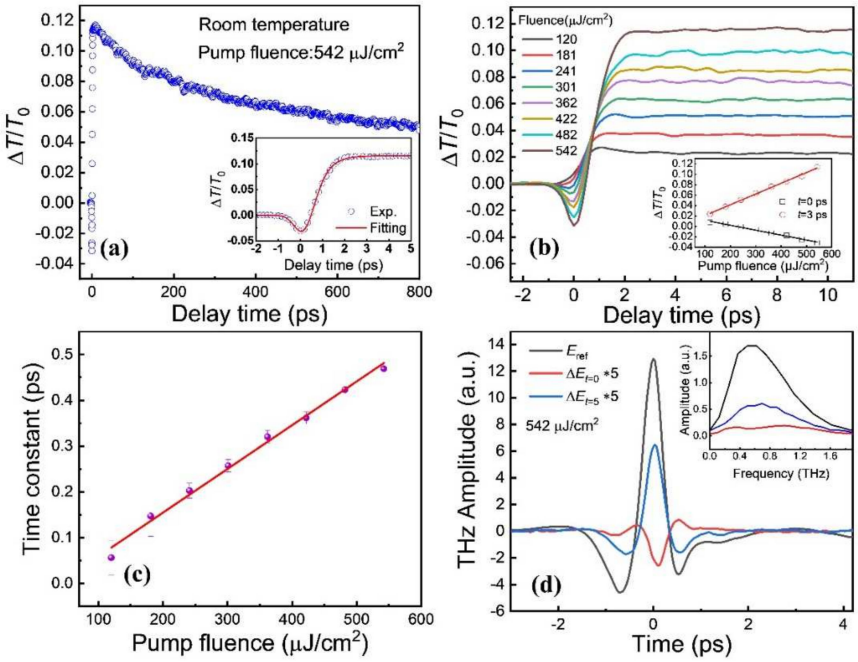


Figure 17. Regulating THz PC by the formation of a small polaron. (**a**) The transient THz transmission in a 20 nm $PtTe_2$ film under 780 nm pump. Inset: zoomed-in transient response in the initial few ps conjunction with a single exponential fitting. (**b**) Transient THz transmission under different pump fluences. Inset: magnitude of $\Delta T/T_0$ at t = 0 ps (black) and t = 3 ps (red) as a function of the pump fluence. (**c**) Time constants of rising component extracted from a single exponential fitting with respect to the pump fluence conjunction with a solid line fitting. (**d**) Transmitted THz waveform without a pump (black) and THz transmission change under a pump fluence of 542 $\mu J/cm^2$ at the delay times t = 0 (red) and t = 5 ps (blue). The corresponding frequency spectra are shown in the inset (Reprinted with permission from Ref. [115]. Copyright 2021, American Physical Society).

Before assigning the negative THz PC to the excitation of a small polaron in the $PtTe_2$ film, authors discussed and ruled out other possible contributions, such as interband scattering, i.e., by exciting a Dirac fermion into a trivial conduction band, formation of trions [114], hot electrons effect [116], impurity effect [117], and THz emission [118]. Then, authors concluded that the photoinduced negative THz PC arises from the photoexcitation-induced formation of a small polaron. Notably, early experimental measurements [119] show that $PtTe_2$ exhibits a strong *e–ph* interaction, with a coupling constant ranging from 0.38 to 0.42. Photogenerated electrons can be strongly coupled to the lattice vibration of $PtTe_2$ under photoexcitation. It is this strong *e–ph* coupling that makes possible the cooling of hot electrons and the deformation of the lattice around the carriers, resulting in small polarons with a reduced mobility. In order to consolidate the photoinduced formation of a small polaron, the authors also performed OPTP studies with varying values of pump fluence, temperature, and $PtTe_2$ film thickness, and all the experimental data supported the formation of a small polaron. The authors also evaluated carrier mobility and the pump-induced mobility change in the 20 nm $PtTe_2$ film in THz frequency. The average carrier mobility μ_0 was calculated to be 1.5 $cm^2\ V^{-1}\ s^{-1}$ based on the THz conductivity and carrier concentration data. The pump-induced carrier mobility change was then obtained to be $\Delta\mu/\mu_0 = (\mu - \mu_0)/\mu_0$ = 10.5% at a delay time of 3 ps under the absorbed photon density of 3.2×10^{14} cm^{-2}. The significantly reduced carrier mobility at a high pumping fluence was indeed consistent with the model of small polaron formation and is due to lattice deformation caused by photogenerated thermal electrons in $PtTe_2$ films.

The photoinduced formation of a small polaron has also been reported by Chen et al. [120] in the low temperature phase of T_d $MoTe_2$ films. The typical results are displayed in Figure 18. After the photoexcitation of 780 nm, the 1T′-phase $MoTe_2$ at a high temperature

exhibits only positive THz PC and its relaxation time is less than 1 ps. When the temperature is lower than 200 K, $MoTe_2$ film undergoes phase transition, from a high temperature 1T′-phase to low temperature T_d-phase $MoTe_2$ [121,122]. While the low-temperature T_d-phase $MoTe_2$ film showed an ultrafast positive THz PC, this was initially followed by a negative THz PC, and the negative THz PC signal lowers to the equilibrium state in the hundreds-of-ps time scale. The authors proposed that small polaron formation induced by hot carrier is ascribed to the negative THz PC in the polar semimetal $MoTe_2$ at a low temperature [120]. The polaron formation time increased slightly with the temperature and was determined to be ~0.4 ps at 5 K and 0.5 ps at 100 K.

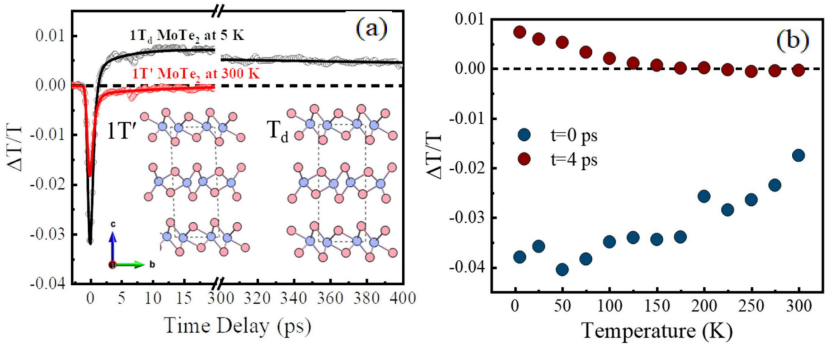


Figure 18. Observation of negative THz PC at a low-temperature-phase $MoTe_2$. (**a**) Transient THz transmission in a semimetal $MoTe_2$ film with a photoexcitation of 780 nm at 5 K and 300 K. The inset shows the molecular structure of high-temperature 1T′-phase and low-temperature T_d-phase. (**b**) Maximum $\Delta T/T_0$ measured at the delay times of Δt = 0 ps (black) and 4 ps (red). The dashed line is the baseline, i.e., $\Delta T/T_0 = 0$ (Reprinted with permission from Ref. [120]. Copyright 2014, American Chemistry Society).

In addition to probing small polaron formation, THz spectroscopy has also been used to investigate the dynamic formation and band transport of large polarons in 2D materials [123–126]. Employing time-resolved THz spectroscopy, Bretschneider et al. [124] studied the temperature- and pump-energy-dependent rising process of THz PC in three organic–inorganic hybrid metal halide perovskites, $CH_3NH_3PbI_3$, $CH(NH_2)_2PbI_3$, and $CsPbI_3$. They found that the rise in PC can be well described by a simple model, in which the initial carrier cooling and large polaron formation occur in succession [124]. The polaron formation time was determined to be ~400 fs for the three investigated perovskite films. Jin et al. [125] demonstrated the use of the OPTP technique to access the nature of the interplay of photoexcited unbound charge carriers and optical phonons in polycrystalline $CH_3NH_3PbI_3$ with a grain size of about 10 μm. By using the Drude–Smith–Lorentz model and Fröhlich-type *e–ph* coupling, they came to the conclusion of the formation of large polarons of a much longer charge lifetime in polycrystalline perovskite films, which is a result of the efficient protection of band-edge carriers by the trap potential and low thermal conductivity. Zheng et al. [126] employed the OPTP technique to investigate the temperature-dependent THz PC of two model MXenes: semiconducting $Nb_4C_3T_x$ and metallic $Ti_3C_2T_x$, in which $Nb_4C_3T_x$ nanoflake behaves as a positive THz PC response, while negative THz PC occurs in $Ti_3C_2T_x$ nanoflake following optical excitation. The experimental results obtained from transient THz PC revealed that the band-like transport dominates the short-range, intra-flake charge transport in MXenes. This is in contrast to previously static electrical transport measurements [127,128], in which inter-flake transport occurs by hopping and becomes the limiting step for charge percolation through the network of MXene flakes. Furthermore, they also reported that carrier-LO phonon scattering plays a dominating role in intra-flake carrier transport for both semiconducting and metallic MXenes [126]. This study reconciled the debate between theoretical and static electrical transport studies on the charge transport mechanism, and a unifying picture was proposed to depict the charge transport in MXenes [126].

As one of most investigated 2D materials, graphene exhibits linear band dispersion, high carrier mobility, and strong light–matter interaction over a broad band frequency. Plasmon in a structured graphene is widely used to regulate the optical response and THz photoconductivity. Graphene plasmonics shows some advantages as compared to metal plasmonics. The plasmonic Drude weight is dominated by the graphene carrier density, which shows a high tunability with electrical field, chemical doping, or optical excitation. The low electronic density of states and relatively weak electron–phonon coupling makes graphene to have very-high carrier mobilities, attainable via graphene enclosed within hBN multilayers. In addition, electromagnetic fields can be confined into a dimension that is much smaller than the wavelength of a photon, which promotes the formation of plasmon–polariton interaction, an elementary excitation originating from strong interactions between photons and plasmon. The tight electromagnetic field confinement and large density of photonic states allows plasmon–polariton to achieve novel and otherwise inaccessible functionalities. Recently, polaritons, including plasmon–polariton interactions, have received great interest in the broad fields of physics, materials science, and photonics for both fundamental research and potential applications [129–131].

7. Conclusions and Perspective

Tailorability, particularity, and easy fabrication are behind the extensive attention that research on 2D vdW materials has received in the past two decades. Although graphene has a weak light absorption, most other 2D materials show a strong absorption in the visible and near infrared regions, and light–graphene interaction can be greatly enhanced by stacking graphene and other 2D materials together. In addition, as the THz waves have a low photon energy, low loss to 2D materials, and high sensitivity to free carriers near the Fermi surface, the THz spectrum becomes an effective means to characterize the charge transfer at the surface of materials in many fields, such as condensed matter physics, materials science, biology, and chemistry. Applying THz PC spectroscopy to 2D materials can reveal the fundamental properties of 2D materials, such as identifying elementary excitation, distinguishing charge transport mechanisms, and scattering mechanism. Regulating THz PC can be realized by designing 2D materials with the desired functionality or stacking different 2D materials together. As a result, THz optoelectronic devices, such as THz modulator, switch, and transistor, can be designed and fabricated. In this review, we comprehensively reviewed the latest progress on the regulation of THz PC in 2D materials from four perspective: (i) the influence of gas absorption on the THz PC in graphene and TMD films; (ii) the effect of electric bias on the THz PC in graphene as well as the influence of substrate-introduced field on the THz PC in the Gr/TMD heterostructure; (iii) impact of photogating on the regulation of THz PC based on the Gr/TMD heterostructure; and (iv) the regulation of THz PC via the photoinduced formation of elementary excitations, such as trion, small polaron, and large polaron.

In this paper, we presented a review focused on the regulation of THz PC based on graphene, TMDs, and Gr/TMD heterostructures. As mentioned in the introduction, the members of 2D materials' family covers from graphene to TMDs, to hBN [10], silicone [11], MXene [12], phosphorene [13], borophene [14], and heterostructures by stacking two or more different 2D materials together [3,7,15,16]. Different 2D materials process diverse structures, properties, and functionalities. Graphene and TMDs are the most-studied candidates in the 2D materials' family. In general, the regulation of THz PC discussed in this paper is applicable to other 2D materials; of course, the detailed THz PC may be different due to the different molecular structure and inter- and/or intralayer interaction. For instance, Zheng et al. revealed that THz PC in Mexene film is dominated by intra-MXene flake transport of charge carrier; this contrasts with the static electric transport measurement, in which inter-flake charge carrier hoppling dominates the charge transport [126].

In addition to the effects of the gas absorption, electrostatic gating, photogating as well as the formation of elementary excitation on the THz PC, other methods, such as strain, magnetic field, and quantum confinement, can also play important roles in regulating THz

PC. Xu et al. predicted with the first principle calculation that 1T′-phase monolayer Janus transition metal dichalcogenides (JTMDs) possess colossal nonlinear photoconductivity. They also revealed that in-plane strain can induce topological phase transitions in the 1T′ JTMDs, and the shift current can abruptly flip their directions [132]. Arora A. et al. demonstrated theoretically that large injection currents can develop in strained, twisted bilayer graphene heterostructures with a broken sublattice symmetry [133]. Akimov et al. presented an overview of optical and photocurrent spectroscopy with picosecond strain pulses [134], in which a picosecond strain pulse can be used to gate, on a picosecond timescale, the photocurrent in a p–i–n diode containing a quantum structure (including quantum well and quantum wires and quantum dots) in its intrinsic region. In addition, magnetic field can also be used to regulate photoconductivity and photocurrent. S. Candussio et al. reported the observation of edge electric currents excited in bilayer graphene by THz laser radiation [135]. The application of a small magnetic field normal to the graphene plane leads to a phase shift in the polarization dependence. The authors also revealed that the photocurrent exhibits sign alternating magneto-oscillations showing periodic in 1/B [135]. In 2D materials, photocarriers are confined in a two-dimensional space, and quantum confinement also plays an important role in regulating the photoconductivity and photocurrent in 2D materials. Silvia G. Motti et al. demonstrated that 2D perovskite $(BA)_2PbI_4$ exhibits surprisingly high in-plane mobilities and enhanced charge–phonon coupling with respect to the 3D counterpart (BEA)2PbI4 [136]. Last but not least, the twist angle of homo-/hetero-bilayer graphene and/or TMD structure can also have a roles in affecting the photocurrent and photoconductivity. Conventionally, introducing Moiré lattice in 2D materials twist angle can localize the carrier transport, which results in decreasing in PC. By constructing the Gr/MoS_2 bilayer with different twist angles, Luo et al. found that the charge transfer timescale from MoS_2 to graphene varies strongly with twist angle, becoming faster for smaller twist angles, and shows that the relaxation timescale is significantly shorter in a heterostructure as compared to a monolayer [137].

Although the non-equilibrium THz PC of 2D materials and vdW heterostructures have been employed to detect the carrier and energy transfer, thermalization kinetic process of the carriers around Fermi surface. However, open questions remain in these series of 2D materials, and heterostructures require extensive in-depth investigation, such as the heat transfer process [138], phonon recycling [139], transient shift current [140,141], and hot electron extraction [135]. In addition, the development of a new time resolved technique, such as the near-field THz imaging, will provide new insights into the understanding of the non-equilibrium dynamics at the angstrom scale 2D material interface. In addition to THz PC spectroscopy, THz emission spectroscopy based on the photoinduced charge current has also been demonstrated to be a powerful tool to study the charge dynamics and charge transfer. For instance, photoexcitation-induced charge transfer in a heterostructure is expected to accompany THz emission arising from the photocurrent [142]. Although a few pieces in the literature reported the observation of THz emission in the TMDs/TMDs heterostructure, there is no report about THz emission in Gr/TMD heterostructures to date, and the underlined mechanism is still not clear at present. Moreover, by fabricating a monolayer TMDs on a ferromagnetic thin film to construct a ferromagnetic heterostructure, the photoexcitation of ferromagnetic layer may lead to spin injection in the TMD layer; as a result, enhanced THz emission could be possible via inverse spin Hall effect [143–146]. In conclusion, transient THz PC spectroscopy assisted with THz emission spectroscopy can provide an insight into the photocarrier dynamics of the desired 2D materials as well as the heterostructures; the regulation of THz PC shows the uttermost important in the fundamental research of 2D materials and the heterostructure, which is also significantly important in designing and developing novel THz optoelectronic devices.

Author Contributions: G.M. supervised the reviewed article; all authors contributed to the writing and revision of the paper. X.X. and Z.Z. contributed equally to the work. All authors have read and agreed to the published version of the manuscript.

Funding: This work was supported by the National Natural Science Foundation of China (NSFC, Nos. 92150101, 92050203, 61735010, 61905264, and 62105347), and the Science and Technology Commission of Shanghai Municipality (Grant No. 21JC1402600).

Institutional Review Board Statement: Not applicable.

Informed Consent Statement: Not applicable.

Data Availability Statement: This is review article, no new data available.

Conflicts of Interest: The authors declare no conflict of interest.

References

1. Novoselov, K.S.; Geim, A.K.; Morozov, S.V.; Jiang, D.; Zhang, Y.; Dubonos, S.V.; Grigorieva, I.V.; Firsov, A.A. Electric field effect in atomically thin carbon films. *Science* **2004**, *306*, 666. [CrossRef]
2. Zhou, Y.; Sung, J.; Brutschea, E.; Esterlis, I.; Wang, Y.; Scuri, G.; Gelly, R.J.; Heo, H.; Taniguchi, T.; Watanabe, K.; et al. Bilayer Wigner crystals in a transition metal dichalcogenide heterostructure. *Nature* **2021**, *595*, 48. [PubMed]
3. Wallbank, J.R.; Ghhazaryan, D.; Misra, A.; Cao, Y.; Tu, J.S.; Piot, B.A.; Potemski, M.; Pezzini, S.; Wiiedmann, S.; Zeitler, U.; et al. Tuning the valley and chiral quantum state of Dirac electrons in van der Waals heterostructures. *Science* **2016**, *353*, 575. [CrossRef] [PubMed]
4. Kar, S.; Lake, J.; Adeyemo, S.O.; Santra, T.S.; Joyce, H.J. The physics of terahertz negative photoconductivity in low dimensional materials. *Mater. Today Phys.* **2022**, *23*, 100631.
5. Sun, Z.; Martinez, A.; Wang, F. Optical modulators with 2D layered materials. *Nat. Photonics* **2016**, *10*, 227.
6. Ahn, C.; Cavalleri, A.; Georges, A.; Ismail-Beigi, S.; Millis, A.J.; Triscone, J. Designing and controlling the properties of transition metal oxide quantum materials. *Nat. Mater.* **2021**, *20*, 1462. [CrossRef]
7. Gong, C.; Zhang, X. Two-dimensional magnetic crystals and emergent heterostructure devices. *Science* **2019**, *363*, 706.
8. Trovatello, C.; Marini, A.; Xu, X.; Lee, C.; Liu, F.; Curreli, N.; Manzoni, C.; Conte, S.D.; Yao, K.; Ciattoni, A.; et al. Optical parametric amplification by monolayer transition metal dichalcogenides. *Nat. Photonics* **2021**, *15*, 6–10. [CrossRef]
9. Mahatha, S.K.; Patel, K.D.; Menon, K.S. Electronic structure investigation of MoS_2 and $MoSe_2$ using angle-resolved photoemission spectroscopy and ab initio band structure studies. *J. Phys. Condens. Matter* **2011**, *24*, 475504. [CrossRef] [PubMed]
10. Wickramaratne, D.; Weston, L.; Van de Walle, C.G. Monolayer to bulk properties of hexagonal boron nitride. *J. Phys. Chem. C* **2018**, *122*, 25524. [CrossRef]
11. Kara, A.; Enriquez, H.; Seitsonen, A.P.; Voon LL, Y.; Vizzini, S.; Aufray, B.; Oughaddou, H. A review on silicene d new candidate for electronics. *Surf. Sci. Rep.* **2012**, *67*, 1–18.
12. Djire, A.; Zhang, H.; Liu, J.; Miller, E.M.; Neale, N.R. Electrocatalytic and optoelectronic characteristics of the two-dimensional titanium nitride $Ti_4N_3T_x$ MXene. *ACS Appl. Mater. Interfaces* **2019**, *11*, 11812. [CrossRef] [PubMed]
13. Wu, M.; Zeng, X.C. Intrinsic Ferroelasticity and/or Multiferroicity in Two-Dimensional Phosphorene and Phosphorene Analogues. *Nano Lett.* **2016**, *16*, 3236. [CrossRef] [PubMed]
14. Ranjan, P.; Ranjan, P.; Lee, J.M.; Kumar, P.; Vinu, A. Borophene: New sensation in flatland. *Adv. Mater.* **2020**, *32*, 2000531. [CrossRef]
15. Schwartz, I.; Shimazaki, Y.; Kuhlenkamp, C.; Watanabe, K.; Taniguchi, T.; Kroner, M.; Imamoglu, A. Electrically tunable Feshbach resonances in twisted bilayer semiconductors. *Science* **2021**, *374*, 336. [CrossRef]
16. Liu, L.; Li, T.; Ma, L.; Li, W.; Gao, S.; Sun, W.; Dong, R.; Zou, X.; Fan, D.; Shao, L.; et al. Uniform nucleation and epitaxy of bilayer molybdenum disulfide on sapphire. *Nature* **2022**, *605*, 69. [CrossRef]
17. Yin, Z.; Li, H.; Li, H.; Jiang, L.; Shi, Y.; Sun, Y.; Lu, G.; Zhang, Q.; Chen, X.; Zhang, H. Single-layer MoS_2 phototransistors. *ACS Nano* **2012**, *6*, 74. [CrossRef] [PubMed]
18. Choi, W.; Cho, M.Y.; Konar, A.; Lee, J.H.; Cha, G.-B.; Hong, S.C.; Kim, S.; Kim, J.; Jena, D.; Joo, J.; et al. High-detectivity multilayer MoS_2 phototransistors with spectral response from ultraviolet to infrared. *Adv. Mater.* **2012**, *24*, 5832. [CrossRef]
19. Tsai, M.L.; Su, S.H.; Chang, J.K.; Tsai, D.S.; Chen, C.H.; Wu, C.I.; Li, L.J.; Chen, L.J.; He, J.H. Monolayer MoS_2 heterojunction solar cells. *ACS Nano* **2014**, *8*, 8317. [CrossRef]
20. Wang, C.; Yang, F.; Gao, Y. The highly-efficient light-emitting diodes based on transition metal dichalcogenides: From architecture to performance. *Nanoscale Adv.* **2020**, *2*, 4323.
21. Lopez-Sanchez, O.; Lembke, D.; Kayci, M.; Radenovic, A.; Kis, A. Ultrasensitive photodetectors based on monolayer MoS_2. *Nat. Nanotechnol.* **2013**, *8*, 497. [CrossRef] [PubMed]
22. Lembke, D.; Bertolazzi, S.; Kis, A. Single-layer MoS_2 electronics. *Acc. Chem. Res.* **2015**, *48*, 100. [CrossRef]
23. Lu, J.; Li, X.; Zhang, Y.; Hwang, H.Y.; Ofori-Okai, B.K.; Nelson, K.A. Two-Dimensional Spectroscopy at Terahertz Frequencies. *Multidimensional Time-Resolved Spectroscopy* **2018**, 275–320. [CrossRef]
24. Li, G.; Li, D.; Jin, Z.; Ma, G. Photocarriers dynamics in silicon wafer studied with optical-pump terahertz-probe spectroscopy. *Opt. Commun.* **2012**, *285*, 4102. [CrossRef]
25. Li, D.; Li, G.; Kong, H.; Shu, S.; Ma, G.; Ge, J.; Hu, S.; Dai, N. The Extraordinary Transmission Spectrum in Terahertz Regime: Combination of Shape Resonances and Rayleigh anomalies. *J. Millim. Infrared THz Waves* **2012**, *33*, 212. [CrossRef]

26. Li, G.; Jin, Z.; Xue, X.; Lin, X.; Ma, G.; Hu, S.; Dai, N. Terahertz coherent control of surface plasmon polariton propagation in subwavelength metallic hole arrays. *Appl. Phys. Lett.* **2012**, *100*, 191115. [CrossRef]
27. Xue, X.; Jiang, M.; Li, G.; Lin, X.; Ma, G.; Jin, P. Photoinduced Insulator-Metal Phase Transition and the Metallic Phase Propagation in VO_2 Films Investigated by Time-Resolved Terahertz Spectroscopy. *J. Appl. Phys.* **2013**, *114*, 193506. [CrossRef]
28. Zhang, W.; Yang, Y.; Suo, P.; Zhao, W.; Guo, J.; Lu, Q.; Lin, X.; Jin, Z.; Wang, L.; Chen, G.; et al. Ultrafast photocarrier dynamics in a 3D Dirac semimetal Cd_3As_2 film studied with terahertz spectroscopy. *Appl. Phys. Lett.* **2019**, *114*, 221102. [CrossRef]
29. Zhang, W.; Guo, J.; Suo, P.; Lv, L.; Liu, J.; Lin, X.; Jin, Z.; Liu, W.; Ma, G. Optically Controlled Ultrafast Terahertz Switching in CdTe Nanostructure Thin Film. *Appl. Opt.* **2019**, *58*, 308200. [CrossRef]
30. Kittel, C. *Introduction to Solid State Physics*, 7th ed.; John Wiley & Sons Ltd.: Hoboken, NJ, USA, 1996.
31. Ulbricht, R.; Hendry, E.; Shan, J.; Heinz, T.F.; Bonn, M. Carrier dynamics in semiconductors studied with time-resolved terahertz spectroscopy. *Rev. Mod. Phys.* **2011**, *83*, 543.
32. Shimakawa, K.; Itoh, T.; Naito, H.; Kasap, S.O. The origin of non-Drude terahertz conductivity in nanomaterials. *Appl. Phys. Lett.* **2012**, *100*, 132102. [CrossRef]
33. Zhang, Y.; Tang, T.-T.; Girit, C.; Hao, Z.; Martin, M.C.; Zettl, A.; Crommie, M.F.; Shen, Y.R.; Wang, F. Direct observation of a widely tunable bandgap in bilayer graphene. *Nature* **2009**, *459*, 820. [CrossRef] [PubMed]
34. George, P.A.; Strait, J.; Dawlaty, J.; Shivaraman, S.; Chandrashekhar, M.; Rana, F.; Spencer, M.G. Ultrafast optical-pump terahertz-probe spectroscopy of the carrier relaxation and recombination dynamics in epitaxial graphene. *Nano Lett.* **2008**, *8*, 4248–4251. [CrossRef] [PubMed]
35. Bahk, Y.M.; Ramakrishnan, G.; Choi, J.; Song, H.; Choi, G.; Kim, Y.H.; Ahn, K.J.; Kim, D.S.; Planken, P.C.M. Plasmon enhanced terahertz emission from single layer graphene. *ACS Nano* **2014**, *8*, 9089–9096. [CrossRef]
36. Ivanov, I.; Bonn, M.; Mics, Z.; Turchinovich, D. Perspective on terahertz spectroscopy of graphene. *Europhys. Lett.* **2015**, *111*, 67001. [CrossRef]
37. Docherty, C.J.; Lin, C.T.; Joyce, H.J.; Nicholas, R.J.; Herz, L.M.; Li, L.J.; Johnston, M.B. Extreme sensitivity of graphene photoconductivity to environmental gases. *Nat. Commun.* **2015**, *3*, 1228. [CrossRef] [PubMed]
38. Zhang, Z.; Lin, T.; Xing, X.; Lin, X.; Meng, X.; Cheng, Z.; Jin, Z.; Ma, G. Photoexcited terahertz conductivity dynamics of graphene tuned by oxygen-adsorption. *Appl. Phys. Lett.* **2017**, *110*, 111108. [CrossRef]
39. Hafez, H.A.; Chai, X.; Sekine, Y.; Takamura, M.; Oguri, K.; Al-Naib, I.; Dignam, M.M.; Hibino, H.; Ozaki, T. Effects of environmental conditions on the ultrafast carrier dynamics in graphene revealed by terahertz spectroscopy. *Phys. Rev. B* **2017**, *95*, 165428. [CrossRef]
40. Mics, Z.; Tielrooij, K.J.; Parvez, K.; Jensen, S.A.; Ivanov, I.; Feng, X.; Müllen, K.; Bonn, M.; Turchinovich, D. Thermodynamic picture of ultrafast charge transport in graphene. *Nat. Commun.* **2015**, *6*, 7655. [CrossRef]
41. Jia, T.; Zhang, W.; Zhang, Z.; Zhan, Z.; Ma, G.; Du, J.; Leng, Y. Role of the Optical Acoustic Phonon Interaction in the Ultrafast Cooling Process of CVD Graphene. *J. Phys. Chem. C* **2021**, *125*, 27283. [CrossRef]
42. Wu, J.; Yue, G.; Chen, W.; Xing, Z.; Wang, J.; Wong, W.R.; Cheng, Z.; Set, S.Y.; Senthil Murugan, G.; Wang, X.; et al. On-Chip Optical Gas Sensors Based on Group-IV Materials. *ACS Photonics* **2020**, *7*, 2923. [CrossRef]
43. Di Bartolomeo, A.; Genovese, L.; Giubileo, F.; Iemmo, L.; Luongo, G.; Foller, T.; Schleberger, M. Hysteresis in the transfer characteristics of MoS_2 transistors 2D Materials. *2D Mater.* **2017**, *5*, 015014. [CrossRef]
44. Lin, Z.; McCreary, A.; Briggs, N.; Subramanian, S.; Zhang, K.; Sun, Y.; Li, X.; Borys, N.J.; Yuan, H.; Fullerton-Shirey, S.K. 2D materials advances: From large scale synthesis and controlled heterostructures to improved characterization techniques, defects and applications. *2D Mater.* **2016**, *3*, 042001. [CrossRef]
45. Yoon, Y.; Ganapathi, K.; Salahuddin, S. How Good Can Monolayer MoS_2 Transistors Be? *Nano Lett.* **2011**, *11*, 3768. [CrossRef] [PubMed]
46. Late, D.J.; Shaikh, P.A.; Khare, R.; Kashid, R.V.; Chaudhary, M.; More, M.A.; Ogale, S.B. Pulsed Laser-Deposited MoS_2 Thin Films on W and Si: Field Emission and Photoresponse Studies. *ACS Appl. Mater. Interfaces* **2014**, *6*, 15881. [CrossRef]
47. Sun, K.; Ma, H.; Xia, W.; Suo, P.; Zhang, W.; Zou, Y.; Lin, X.; Zhang, S.; Guo, Y.; Ma, G. Dynamical Response of Nonlinear Optical Anisotropy in a Tin Sulfide Crystal under Ultrafast Photoexcitation. *J. Phys. Chem. Lett.* **2022**, *13*, 9355–9362. [CrossRef]
48. Peimyoo, N.; Yang, W.; Shang, J.; Shen, X.; Wang, Y.; Yu, T. Chemically Driven Tunable Light Emission of Charged and Neutral Excitons in Monolayer WS_2. *ACS Nano* **2014**, *8*, 11320. [CrossRef]
49. Kobayashi, Y.; Sasaki, S.; Mori, S.; Hibino, H.; Liu, Z.; Watanabe, K.; Taniguchi, T.; Suenaga, K.; Maniwa, Y.; Miyata, Y. Growth and Optical Properties of High-Quality Monolayer WS_2 on Graphite. *ACS Nano* **2015**, *9*, 4056. [CrossRef]
50. Raja, A.; Chaves, A.; Yu, J.; Arefe, G.; Hill, H.M.; Rigosi, A.F.; Berkelbach, T.C.; Nagler, P.; Schüller, C.; Korn, T.; et al. Coulomb engineering of the bandgap and excitons in two-dimensional materials. *Nat. Commun.* **2017**, *8*, 15251. [CrossRef]
51. Krasnok, A.; Lepeshov, S.; Alú, A. Nanophotonics with 2D transition metal dichalcogenides. *Opt. Express* **2018**, *26*, 15972. [CrossRef]
52. Urban, F.; Martucciello, N.; Peters, L.; McEvoy, N.; Bartolomeo, A.D. Environmental Effects on the Electrical Characteristics of Back-Gated WSe_2 Field-Effect Transistors. *Nanomaterials* **2018**, *8*, 901. [CrossRef] [PubMed]
53. Bartolomeo, A.D.; Pelella, A.; Liu, X.; Miao, F.; Passacantando, M.; Giubileo, F.; Grillo, A.; Iemmo, L.; Urban, F.; Liang, S.J. Pressure-Tunable Ambipolar Conduction and Hysteresis in Thin Palladium Diselenide Field Effect Transistors. *Adv. Funct. Mater.* **2019**, *29*, 1902483. [CrossRef]

54. Li, H.; Yin, Z.; He, Q.; Li, H.; Huang, X.; Lu, G.; Fam, D.W.H.; Tok, A.I.Y.; Zhang, Q.; Zhang, H. Fabrication of Single- and Multilayer MoS_2 Film-Based Field-Effect Transistors for Sensing NO at Room Temperature. *Small* **2012**, *8*, 63. [CrossRef] [PubMed]
55. Urban, F.; Giubileo, F.; Grillo, A.; Iemmo, L.; Luongo, G.; Passacantando, M.; Foller, T.; Madauß, L.; Pollmann, E.; Geller, M.P.; et al. Gas dependent hysteresis in MoS_2 field effect transistors. *2D Mater.* **2019**, *6*, 045049. [CrossRef]
56. Park, W.; Park, J.; Jang, J.; Lee, H.; Jeong, H.; Cho, K.; Hong, S.; Lee, T. Oxygen environmental and passivation effects on molybdenum disulfide field effect transistors. *Nanotechnology* **2013**, *24*, 095202. [CrossRef]
57. Qiu, H.; Pan, L.; Yao, Z.; Li, J.; Shi, Y.; Wang, X. Electrical characterization of back-gated bi-layer MoS_2 field-effect transistors and the effect of ambient on their performances. *Appl. Phys. Lett.* **2012**, *100*, 123104. [CrossRef]
58. Grillo, A.; Faella, E.; Pelella, A.; Giubileo, F.; Ansari, L.; Gity, F.; Hurley, P.K.; McEvoy, N.; Bartolomeo, A.D. Coexistence of Negative and Positive Photoconductivity in Few-Layer $PtSe_2$ Field-Effect Transistors. *Adv. Funct. Mater.* **2021**, *31*, 2105722. [CrossRef]
59. Lee, Y.-H.; Zhang, X.-Q.; Zhang, W.; Chang, M.-T.; Lin, C.-T.; Chang, K.-D.; Yu, Y.-C.; Wang, J.T.-W.; Chang, C.-S.; Li, L.-J.; et al. Synthesis of Large-Area MoS_2 Atomic Layers with Chemical Vapor Deposition. *Adv. Mater.* **2012**, *24*, 2320. [CrossRef]
60. Zhang, W.; Huang, J.-K.; Chen, C.-H.; Chang, Y.-H.; Cheng, Y.-J.; Li, L.-J. High-Gain Phototransistors Based on a CVD MoS_2 Monolayer. *Adv. Mater.* **2013**, *25*, 3456. [CrossRef]
61. Hornett, S.M.; Heath, M.; Horsell, D.W.; Hendry, E. Optically induced oxygen desorption from graphene measured using femtosecond two-pulse correlation. *Phys. Rev. B* **2014**, *90*, 081401. [CrossRef]
62. Wang, H.I.; Braatz, M.-L.; Richter, N.; Tielrooij, K.-J.; Mics, Z.; Lu, H.; Weber, N.-E.; Müllen, K.; Turchinovich, D.; Kläui, M.; et al. Reversible Photochemical Control of Doping Levels in Supported Graphene. *J. Phys. Chem. C* **2017**, *121*, 4083. [CrossRef]
63. Tongay, S.; Suh, J.; Ataca, C.; Fan, W.; Luce, A.; Kang, J.S.; Liu, J.; Ko, C.; Raghunathanan, R.; Zhou, J.; et al. Defects activated photoluminescence in two-dimensional semiconductors: Interplay between bound; charged and free excitons. *Sci. Rep.* **2013**, *3*, 2657. [CrossRef] [PubMed]
64. Tongay, S.; Zhou, J.; Ataca, C.; Liu, J.; Kang, J.S.; Matthews, T.S.; You, L.; Li, J.; Grossman, J.C.; Wu, J. Broad-Range Modulation of Light Emission in Two-Dimensional Semiconductors by Molecular Physisorption Gating. *Nano Lett.* **2013**, *13*, 2831. [CrossRef] [PubMed]
65. Nan, H.; Wang, Z.; Wang, W.; Liang, Z.; Lu, Y.; Chen, Q.; He, D.; Tan, P.; Miao, F.; Wang, X.; et al. Strong Photoluminescence Enhancement of MoS_2 through Defect Engineering and Oxygen Bonding. *ACS Nano* **2014**, *8*, 5738. [CrossRef] [PubMed]
66. Gogoi, P.K.; Hu, Z.; Wang, Q.; Carvalho, A.; Schmidt, D.; Yin, X.; Chang, Y.-H.; Li, L.-J.; Sow, C.H.; Neto, A.H.C.; et al. Oxygen Passivation Mediated Tunability of Trion and Excitons in MoS_2. *Phys. Rev. Lett.* **2017**, *119*, 077402. [CrossRef]
67. Xing, X.; Zhao, L.; Zhang, Z.; Lin, X.; Yu, Y.; Jin, Z.; Liu, W.; Zhang, W.; Ma, G. The modulation of terahertz photoconductivity in CVD grown n-doped monolayer MoS_2 with gas adsorption. *J. Phys. Condens. Matter* **2019**, *31*, 245001. [CrossRef]
68. Kim, J.H.; Lee, J.; Kim, J.H.; Hwang, C.C.; Lee, C.; Park, J.Y. Work function variation of MoS_2 atomic layers grown with chemical vapor deposition: The effects of thickness and the adsorption of water/oxygen molecules. *Appl. Phys. Lett.* **2015**, *106*, 251606. [CrossRef]
69. Late, D.J.; Liu, B.; Matte, H.S.S.R.; Dravid, V.P.; Rao, C.N.R. Hysteresis in Single-Layer MoS_2 Field Effect Transistors. *ACS Nano* **2012**, *6*, 5635. [CrossRef]
70. Gustafson, J.K.; Wines, D.; Gulian, E.; Ataca, C.; Hayden, L.M. Positive and Negative Photoconductivity in Monolayer MoS_2 as a Function of Physisorbed Oxygen. *J. Phys. Chem. C* **2021**, *125*, 8712. [CrossRef]
71. Mak, K.F.; Mak, K.F.; Sfeir, M.Y.; Wu, Y.; Lui, C.H.; Misewich, J.A.; Heinz, T.F. Measurement of the Optical Conductivity of Graphene. *Phys. Rev. Lett.* **2008**, *101*, 196405. [CrossRef]
72. Wang, F.; Zhang, Y.B.; Tian, C.S.; Girit, C.; Zettl, A.; Crommie, M.; Shen, Y.R. Gate-variable optical transitions in graphene. *Science* **2008**, *320*, 208. [CrossRef] [PubMed]
73. Choi, H.; Borondics, F.; Siegel, D.A.; Zhou, S.Y.; Martin, M.C.; Lanzara, A.; Kaindl, R.A. Broadband electromagnetic response and ultrafast dynamics of few-layer epitaxial graphene. *Appl. Phys. Lett.* **2009**, *94*, 172104. [CrossRef]
74. Tielrooij, K.J.; Song, J.C.W.; Jensen, S.A.; Centeno, A.; Pesquera, A.; Elorza, A.Z.; Bonn, M.; Levitov, L.S.; Koppens, F.H.L. Photoexcitation cascade and multiple hot-carrier generation in graphene. *Nat. Phys.* **2013**, *9*, 248. [CrossRef]
75. Hattab, H.; N'Diaye, A.; Wall, D.; Klein, C.; Jnawali, G.; Coraux, J.; Busse, C.; van Gastel, R.; Poelsema, B.; Michely, T.; et al. Interplay of Wrinkles, Strain, and Lattice Parameter in Graphene on Iridium. *Nano Lett.* **2012**, *3*, 1228. [CrossRef] [PubMed]
76. Frenzel, A.J.; Lui, C.H.; Fang, W.; Nair, N.L.; Herring, P.K.; Jarillo-Herrero, P.; Kong, J.; Gedik, N. Observation of suppressed terahertz absorption in photoexcited graphene. *Appl. Phys. Lett.* **2013**, *102*, 113111. [CrossRef]
77. Svintsov, D.; Otsuji, T.; Mitin, V.; Shur, M.S.; Ryzhii, V. Negative terahertz conductivity in disordered graphene bilayers with population inversion. *Appl. Phys. Lett.* **2015**, *106*, 113501. [CrossRef]
78. Frenzel, A.J.; Lui, C.H.; Shin, Y.C.; Kong, J.; Gedik, N. Semiconducting-to-metallic Photoconductivity Crossover and Temperature-Dependent Drude Weight in Graphene. *Phys. Rev. Lett.* **2014**, *113*, 056602. [CrossRef]
79. Shi, S.F.; Tang, T.T.; Zeng, B.; Ju, L.; Zhou, Q.; Zettl, A.; Wang, F. Controlling Graphene Ultrafast Hot carrier Response from Metal-like to Semiconductor-like by Electrostaic Gating. *Nano Lett.* **2014**, *14*, 1578. [CrossRef]
80. Tomadin, A.; Hornett, S.M.; Wang, H.I.; Alexeev, E.M.; Candini, A.; Coletti, C.; Turchinovich, D.; Klaui, M.; Bonn, M.; Koppens, F.H.L.; et al. The ultrafast dynamics and conductivity of photoexcited graphene at different Fermi energies. *Sci. Adv.* **2018**, *4*, eear5313. [CrossRef]

81. Cowley, A.M.; Sze, S.M. Surface States and Barrier Height of Metal-Semiconductor Systems. *J. Appl. Phys.* **1965**, *36*, 3212. [CrossRef]
82. Tung, R.T. The physics and chemistry of the Schottky barrier height. *Appl. Phys. Rev.* **2014**, *1*, 011304. [CrossRef]
83. Sun, D.; Aivazian, G.; Jones, A.M.; Ross, J.S.; Yao, W.; Cobden, D.; Xu, X.D. Ultrafast hot-carrier-dominated photocurrent in graphene. *Nat. Nanotechnol.* **2012**, *7*, 114. [CrossRef]
84. Fiori, G.; Bonaccorso, F.; Iannaccone, G.; Palacios, T.; Neumaier, D.; Seabaugh, A.; Banerjee, S.K.; Colombo, L. Electronics based on two-dimensional materials. *Nat. Nanotechnol.* **2014**, *9*, 768. [CrossRef] [PubMed]
85. Liu, Y.; Guo, J.; Zhu, E.B.; Liao, L.; Lee, S.J.; Ding, M.; Shakir, I.; Gambin, V.; Huang, Y.; Duan, X.F. Approaching the Schottky-Mott limit in van der Waals metal-semiconductor junctions. *Nature* **2018**, *557*, 696. [CrossRef] [PubMed]
86. Vu, Q.A.; Shin, Y.S.; Kim, Y.R.; Nguyen, V.L.; Kang, W.T.; Kim, H.; Luong, D.H.; Lee, I.M.; Lee, K.; Ko, D.S.; et al. Two-terminal floating-gate memory with van der Waals heterostructures for ultrahigh on/off ratio. *Nat. Commun.* **2016**, *7*, 12725. [CrossRef]
87. Novoselov, K.S.; Fal'Ko, V.I.; Colombo, L.; Gellert, P.R.; Schwab, M.G.; Kim, K.A. roadmap for graphene. *Nature* **2012**, *490*, 192. [CrossRef]
88. Geim, A.K.; Novoselov, K.S. The rise of graphene. *Nat. Mater.* **2007**, *6*, 183. [CrossRef]
89. Novoselov, K.S.; Geim, A.K.; Morozov, S.V.; Jiang, D.; Katsnelson, M.I.; Grigorieva, I.V.; Dubonos, S.V.; Firsov, A.A. Two-dimensional gas of massless Dirac fermions in graphene. *Nature* **2009**, *438*, 197. [CrossRef]
90. Castro Neto, A.H.; Guinea, F.; Peres, N.M.R.; Novoselov, K.S.; Geim, A.K. The electronic properties of graphene. *Rev. Mod. Phys.* **2009**, *81*, 109. [CrossRef]
91. Yu, W.J.; Li, Z.; Zhou, H.L.; Chen, Y.; Wang, Y.; Huang, Y.; Duan, X.F. Vertically stacked multi-heterostructures of layered materials for logic transistors and complementary inverters. *Nat. Mater.* **2013**, *12*, 246. [CrossRef]
92. Sup Choi, M.; Lee, G.H.; Yu, Y.J.; Lee, D.Y.; Lee, S.H.; Kim, P.; Hone, J.; Yoo, W.J. Controlled charge trapping by molybdenum disulphide and graphene in ultrathin heterostructured memory devices. *Nat. Commun.* **2013**, *4*, 1624. [CrossRef] [PubMed]
93. Zheng, J.; Li, E.L.; Ma, D.M.; Cui, Z.; Peng, T.; Wang, X.L. Effect on Schottky Barrier of Graphene/WS2 Heterostructure with Vertical Electric Field and Biaxial Strain. *Phys. Status Solidi (b)* **2019**, *256*, 1900161. [CrossRef]
94. Yu, Z.G.; Zhang, Y.W.; Yakobson, B.I. Strain-Robust and Electric Field Tunable Band Alignments in van der Waals WSe_2–Graphene Heterojunctions. *J. Phys. Chem. C* **2016**, *120*, 22702. [CrossRef]
95. Sun, M.; Chou, J.P.; Yu, J.; Tang, W.C. Effects of structural imperfection on the electronic properties of graphene/WSe_2 heterostructures. *J. Mater. Chem. C* **2017**, *5*, 10383. [CrossRef]
96. Zhang, W.; Chuu, C.P.; Huang, J.K.; Chen, C.H.; Tsai, M.L.; Chang, Y.H.; Liang, C.T.; Chen, Y.Z.; Chueh, Y.L.; He, J.H. Ultrahigh-Gain Photodetectors Based on Atomically Thin Graphene-MoS_2 Heterostructures. *Sci. Rep.* **2014**, *4*, 3826. [CrossRef]
97. Zhang, L.; Chen, Z.F.; Zhang, R.; Tan, Y.; Wu, T.; Shalaby, M.; Xie, R.; Xu, J.B. Direct Observation of Charge Injection of Graphene in the Graphene/WSe_2 Heterostructure by Optical-Pump Terahertz-Probe Spectroscopy. *ACS Appl. Mater. Interfaces* **2019**, *11*, 47501. [CrossRef] [PubMed]
98. Chen, Y.; Li, Y.J.; Zhao, Y.D.; Zhou, H.Z.; Zhu, H.M. Highly efficient hot electron harvesting from graphene before electron-hole thermalization. *Sci. Adv.* **2019**, *5*, eaax9958. [CrossRef]
99. Froehlicher, G.E.; Lorchat, E.; Berciaud, S. Charge Versus Energy Transfer in Atomically Thin Graphene-Transition Metal Dichalcogenide van der Waals Heterostructures. *Phys. Rev. X* **2018**, *8*, 011007. [CrossRef]
100. Larentis, S.; Tolsma, J.R.; Fallahazad, B.; Dillen, D.C.; Kim, K.; MacDonald, A.H.; Tutuc, E. Band Offset and Negative Compressibility in Graphene-MoS_2 Heterostructures. *Nano Lett.* **2014**, *14*, 2039. [CrossRef]
101. Xing, X.; Zhang, Z.Y.; Quan, C.J.; Zhao, L.T.; Wang, C.W.; Jia, T.Y.; Ren, J.F.; Du, J.; Leng, Y.X. Tunable ultrafast electron transfer in WSe_2–graphene heterostructures enabled by atomic stacking order. *Nanoscale* **2022**, *14*, 7418. [CrossRef]
102. Ma, Q.S.; Zhang, W.J.; Wang, C.W.; Pu, R.H.; Ju, C.W.; Lin, X.; Zhang, Z.Y.; Liu, W.M.; Li, R.X. Hot Carrier Transfer in a Graphene/$PtSe_2$ Heterostructure Tuned by a Substrate-Introduced Effective Electric Field. *J. Phys. Chem. C* **2021**, *125*, 9296. [CrossRef]
103. Xing, X.; Zhao, L.T.; Zhang, W.J.; Wang, Z.; Su, H.M.; Chen, H.Y.; Ma, G.H.; Dai, J.F.; Zhang, W.J. Influence of a substrate on ultrafast interfacial charge transfer and dynamical interlayer excitons in monolayer WSe_2/graphene heterostructures. *Nanoscale* **2020**, *12*, 2498. [CrossRef] [PubMed]
104. Fu, S.; du Fosse, I.; Jia, X.Y.; Xu, J.Y.; Yu, X.Q.; Zhang, H.; Zheng, W.H.; Krasel, S.; Chen, Z.P.; Wang, Z.M.M.; et al. Long-lived charge separation following pump-wavelength-dependent ultrafast charge transfer in graphene/WS2 heterostructures. *Sci. Adv.* **2021**, *7*, eabd9061. [CrossRef] [PubMed]
105. Quan, C.; Xing, X.; Jia, T.; Zhang, Z.; Wang, C.; Huang, S.; Liu, Z.; Du, J.; Leng, Y. Hot Carrier Transfer in PtSe2/Graphene Enabled by the Hot Phonon Bottleneck. *J. Phys. Chem. Lett.* **2022**, *13*, 9456–9463. [CrossRef]
106. Zou, Y.; Ma, Q.S.; Zhang, Z.; Pu, R.; Zhang, W.; Suo, P.; Sun, K.; Chen, J.; Li, D.; Ma, H. Observation of Ultrafast Interfacial Exciton Formation and Relaxation in Graphene/MoS_2 Heterostructure. *J. Phys. Chem. Lett.* **2022**, *13*, 5123–5130. [CrossRef]
107. Kim, H.J.; Lee, K.J.; Park, J.; Shin, G.H.; Park, H.; Yu, K.; Choi, S.Y. Photoconductivity switching in MoTe2/graphene heterostructure by trap-assisted photogating. *ACS Appl. Mater. Interfaces* **2020**, *12*, 38563–38569. [CrossRef]
108. Qiu, D.Y.; Da Jornada, F.H.; Louie, S.G. Optical spectrum of MoS_2: Many-body effects and diversity of exciton states. *Phys. Rev. Lett.* **2013**, *111*, 216805. [CrossRef]

109. He, K.; Kumar, N.; Zhao, L.; Wang, Z.; Mak, K.F.; Zhao, H.; Shan, J. Tightly bound excitons in monolayer WSe_2. *Phys. Rev. Lett.* **2014**, *113*, 026803. [CrossRef]
110. Chernikov, A.; Berkelbach, T.C.; Hill, H.M.; Rigosi, A.; Li, Y.; Aslan, B.; Reichman, D.R.; Hybertsen, M.S.; Heinz, T.F. Exciton binding energy and nonhydrogenic Rydberg series in monolayer WS_2. *Phys. Rev. Lett.* **2014**, *113*, 076802. [CrossRef]
111. Singh, A.; Moody, G.; Wu, S.; Wu, Y.; Ghimire, N.J.; Yan, J.; Mandrus, D.G.; Xu, X.; Li, X. Coherent electronic coupling in atomically thin $MoSe_2$. *Phys. Rev. Lett.* **2014**, *112*, 216804. [CrossRef]
112. Hichri, A.; Amara, I.B.; Ayari, S.; Jaziri, S. Dielectric environment and/or random disorder effects on free, charged and localized excitonic states in monolayer WS_2. *J. Phys. Condens. Matter.* **2017**, *29*, 435305. [CrossRef]
113. Tu, J.S.; Borghardt, S.; Grützmacher, D.; Kardynał, B.E. Experimental observation of a negative grey trion in an electron-rich WSe_2 monolayer. *J. Phys. Condens. Matter.* **2019**, *31*, 415701. [CrossRef] [PubMed]
114. Lui, C.; Frenzel, A.; Pilon, D.; Lee, Y.H.; Ling, X.; Akselrod, G.; Kong, J.; Gedik, N. Trion-induced negative photoconductivity in monolayer MoS_2. *Phys. Rev. Lett.* **2014**, *113*, 166801. [CrossRef] [PubMed]
115. Suo, P.; Zhang, H.; Yan, S.; Zhang, W.; Fu, J.; Lin, X.; Hao, S.; Jin, Z.; Zhang, Y.; Zhang, C. Observation of negative terahertz photoconductivity in large area type-II Dirac semimetal $PtTe_2$. *Phys. Rev. Lett.* **2021**, *126*, 227402. [CrossRef]
116. Ishida, Y.; Masuda, H.; Sakai, H.; Ishiwata, S.; Shin, S. Revealing the ultrafast light-to-matter energy conversion before heat diffusion in a layered Dirac semimetal. *Phys. Rev. B* **2016**, *93*, 100302. [CrossRef]
117. Baek, E.; Rim, T.; Schütt, J.; Baek, C.K.; Kim, K.; Baraban, L.; Cuniberti, G. Negative photoconductance in heavily doped Si nanowire field-effect transistors. *Nano Lett.* **2017**, *17*, 6727–6734. [CrossRef] [PubMed]
118. Yang, Y.; Peng, X.; Hyatt, S.; Yu, D. Broadband quantum efficiency enhancement in high index nanowire resonators. *Nano Lett.* **2015**, *15*, 3541–3546. [CrossRef]
119. Anemone, G.; Garnica, M.; Zappia, M.; Aguilar, P.C.; Al Taleb, A.; Kuo, C.N.; Lue, C.S.; Politano, A.; Benedek, G.; De Parga, A.L.V. Experimental determination of surface thermal expansion and electron–phonon coupling constant of 1T-PtTe2. *2D Mater.* **2020**, *7*, 025007. [CrossRef]
120. Chen, J.; Suo, P.; Zhang, W.; Ma, H.; Fu, J.; Li, D.; Lin, X.; Yan, X.; Liu, W.; Jin, Z. Photocarrier-Driven Emergence of Negative Photoconductivity in Semimetal MoTe2 Films Revealed with Terahertz Spectroscopy. *J. Phys. Chem. C* **2022**, *126*, 9407–9415. [CrossRef]
121. Kim, H.J.; Kang, S.H.; Hamada, I.; Son, Y.W. Origins of the structural phase transitions in $MoTe_2$ and WTe_2. *Phys. Rev. B* **2017**, *95*, 180101. [CrossRef]
122. Cheon, Y.; Lim, S.Y.; Kim, K.; Cheong, H. Structural phase transition and interlayer coupling in few-layer 1T′ and Td $MoTe_2$. *ACS Nano* **2021**, *15*, 2962–2970. [CrossRef] [PubMed]
123. Zhu, H.; Miyata, K.; Fu, Y.; Wang, J.; Joshi, P.P.; Niesner, D.; Williams, K.W.; Jin, S.; Zhu, X.Y. Screening in crystalline liquids protects energetic carriers in hybrid perovskites. *Science* **2016**, *353*, 1409–1413. [CrossRef] [PubMed]
124. Bretschneider, S.A.; Ivanov, I.; Wang, H.I.; Miyata, K.; Zhu, X.; Bonn, M. Quantifying polaron formation and charge carrier cooling in lead-iodide perovskites. *Adv. Mater.* **2018**, *30*, 1707312. [CrossRef]
125. Jin, Z.; Peng, Y.; Fang, Y.; Ye, Z.; Fan, Z.; Liu, Z.; Bao, X.; Gao, H.; Ren, W.; Wu, J. Photoinduced large polaron transport and dynamics in organic–inorganic hybrid lead halide perovskite with terahertz probes. *Light Sci. Appl.* **2022**, *11*, 209. [CrossRef]
126. Zheng, W.; Sun, B.; Li, D.; Gali, S.M.; Zhang, H.; Fu, S.; Di Virgilio, L.; Li, Z.; Yang, S.; Zhou, S. Band transport by large Fröhlich polarons in MXenes. *Nat. Phys.* **2022**, *18*, 544–550. [CrossRef]
127. Lipatov, A.; Alhabeb, M.; Lu, H.; Zhao, S.; Loes, M.J.; Vorobeva, N.S.; Dall'Agnese, Y.; Gao, Y.; Gruverman, A.; Gogotsi, Y. Electrical and elastic properties of individual single-layer Nb4C3Tx MXene flakes. *Adv. Electron. Mater.* **2020**, *6*, 1901382. [CrossRef]
128. Halim, J.; Moon, E.J.; Eklund, P.; Rosen, J.; Barsoum, M.W.; Ouisse, T. Variable range hopping and thermally activated transport in molybdenum-based MXenes. *Phys. Rev. B* **2018**, *98*, 104202. [CrossRef]
129. Paul, K.K.; Kim, J.H.; Lee, Y.H. Hot carrier photovoltaics in van der Waals heterostructures. *Nat. Rev. Phys.* **2021**, *3*, 178–192. [CrossRef]
130. Rivera, N.; Kaminer, I. Light–matter interactions with photonic quasiparticles. *Nat. Rev. Phys.* **2020**, *2*, 538–561. [CrossRef]
131. Cai, Z.; Xu, Y.; Wang, C.; Liu, Y. Polariton photonics using structured metals and 2D materials. *Adv. Opt. Mater.* **2020**, *8*, 1901090. [CrossRef]
132. Xu, H.; Wang, H.; Zhou, J.; Guo, Y.; Kong, J.; Li, J. Colossal switchable photocurrents in topological Janus transition metal dichalcogenides. *npj Comput. Mater.* **2021**, *7*, 31. [CrossRef]
133. Arora, A.; Kong, J.F.; Song, J.C. Strain-induced large injection current in twisted bilayer graphene. *Phys. Rev. B* **2021**, *104*, L241404. [CrossRef]
134. Akimov, A.V.; Scherbakov, A.V.; Yakovlev, D.R.; Bayer, M.; Kent, A. Optical and photocurrent spectroscopy with picosecond strain pulses. *J. Lumin.* **2011**, *131*, 404–408. [CrossRef]
135. Candussio, S.; Durnev, M.V.; Tarasenko, S.A.; Yin, J.; Keil, J.; Yang, Y.; Son, S.K.; Mishchenko, A.; Plank, K.; Bel'kov, V.V.; et al. Edge photocurrent driven by terahertz electric field in bilayer graphene. *Phys. Rev. B* **2020**, *102*, 045406. [CrossRef]
136. Motti, S.G.; Kober-Czerny, M.; Righetto, M.; Holzhey, P.; Smith, J.; Kraus, H.; Snaith, H.J.; Johnston, M.B.; Herz, L.M. Exciton Formation Dynamics and Band-Like Free Charge-Carrier Transport in 2D Metal Halide Perovskite Semiconductors. *Adv. Funct. Mater.* **2023**, 2300363. [CrossRef]

137. Luo, D.; Tang, J.; Shen, X.Z.; Ji, F.H.; Yang, J.; Weathersby, S.; Kozina, M.E.; Chen, Z.J.; Xiao, J.; Ye, Y.S.; et al. Twist-Angle-Dependent Ultrafast Charge Transfer in MoS_2-Graphene van der Waals Heterostructures. *Nano Lett.* **2021**, *21*, 8051–8057. [CrossRef] [PubMed]
138. Fiore, S.; Luisier, M. Ab initio modeling of thermal transport through van der Waals materials. *Phys. Rev. Mater.* **2020**, *4*, 049005. [CrossRef]
139. Wu, S.F.; Yan, T.; Kuai, Z.H.; Pan, W.G. Thermal conductivity enhancement on phase change materials for thermal energy storage: A review. *Energy Storage Mater.* **2020**, *25*, 251. [CrossRef]
140. Suo, P.; Xia, W.; Zhang, W.J.; Zhu, X.; Fu, J.; Lin, X.; Jin, Z.M.; Liu, W.M.; Guo, Y.F.; Ma, G. Terahertz emission on the surface of a van der Waals magnet $CrSiTe_3$. *Laser Photonics Rev.* **2020**, *14*, 200025. [CrossRef]
141. Cao, X.Q.; Huang, Y.Y.; Xi, Y.Y.; Lei, Z.; Du, W.Y.; Han, T.T.; Wang, J.; Wang, H.; Chang, J.W.; Zhu, L.P.; et al. Interplay between Ultrafast Shift Current and Ultrafast Photon Drag Current in Tellurium Nanotubes. *ACS Photonics* **2022**, *9*, 3144. [CrossRef]
142. Wang, L.; Wang, Z.; Wang, H.Y.; Grinblat, G.; Huang, Y.L.; Wang, D.; Ye, X.H.; Li, X.B.; Bao, Q.L.; Wee, A.S.; et al. Slow cooling and efficient extraction of C-exciton hot carriers in MoS_2 monolayer. *Nat. Commun.* **2017**, *8*, 13906. [CrossRef] [PubMed]
143. Yang, J.; Jiang, S.L.; Xie, J.F.; Jiang, H.C.; Xu, S.J.; Zhang, K.; Shi, Y.P.; Zhang, Y.F.; Zeng, Z.; Fang, G.Y.; et al. Identifying the Intermediate Free-Carrier Dynamics Across the Charge Separation in Monolayer $MoS_2/ReSe_2$ Heterostructures. *ACS Nano* **2021**, *15*, 16760. [CrossRef] [PubMed]
144. Zhang, S.N.; Jin, Z.M.; Zhu, Z.D.; Zhu, W.H.; Zhang, Z.Z.; Ma, G.H.; Yao, J.Q. Bursts of efficient terahertz radiation with saturation effect from metalbased ferromagnetic heterostructures. *J. Phys. D Appl. Phys.* **2018**, *51*, 034001. [CrossRef]
145. Jin, Z.M.; Li, J.G.; Zhang, W.J.; Guo, C.Y.; Wan, C.H.; Han, X.F.; Cheng, Z.X.; Zhang, C.; Balakin, A.V.; Shkurinov, A.P.; et al. Magnetic modulation of terahertz waves via spin-polarized electron tunneling based on magnetic tunnel junctions. *Phys. Rev. Appl.* **2020**, *14*, 014032. [CrossRef]
146. Li, C.; Fang, B.; Zhang, L.K.; Chen, Q.; Xie, X.N.; Xu, N.; Zeng, Z.M.; Wang, Z.Y.; Fang, L.; Jiang, T. Studying spin–charge conversion using terahertz pulses. *APL Mater.* **2021**, *9*, 070902.

Disclaimer/Publisher's Note: The statements, opinions and data contained in all publications are solely those of the individual author(s) and contributor(s) and not of MDPI and/or the editor(s). MDPI and/or the editor(s) disclaim responsibility for any injury to people or property resulting from any ideas, methods, instructions or products referred to in the content.